

Search for VBF produced EW gauginos in events with 2 hadronically decaying τ -leptons.

**Dissertation
zur Erlangung des Doktorgrades
des Departement Physik der Universität Hamburg**

vorgelegt von

Daniele Marconi

Hamburg

2015

Gutachter der Dissertation: Prof. Dr. Christian Sander
Prof. —

Gutachter der Disputation: Prof. Dr. Christian Sander
Prof. —
Prof. —
Prof. —

Abstract

Abriss

Contents

1	Introduction	1
2	Theory	2
2.1	The Standard Model of Particle Physics	2
2.2	Supersymmetry	4
2.2.1	Motivations	4
2.2.2	The MSSM	4
2.2.3	SUSY Signatures at the LHC	4
3	The Experimental Setup	6
3.1	The Large Hadron Collider	6
3.2	The CMS Experiment	9
3.2.1	The Magnet	11
3.2.2	Inner tracking system	12
3.2.3	The Electromagnetic calorimeter	14
3.2.4	The Hadron calorimeter	16
3.2.5	The Muon System	18
3.2.6	The Trigger System	19
3.2.7	Software and Computing	20
3.2.7.1	Tier-0	21
3.2.7.2	Tier 1	21
3.2.7.3	Tier 2	21
3.2.7.4	Tier 3	21
4	Search for SUSY in Vector Boson Fusion Processes at the LHC	22
4.1	Introduction	22
4.2	Search Strategy	22
5	Objects Reconstruction	26
5.1	The Particle Flow Algorithm	26
5.2	The Tau Lepton reconstruction	28
5.3	The Jet reconstruction	29
6	Search for VBF SUSY in the di-τ_h Like Sign channel	30
6.1	The Analysis Strategy	30
6.1.1	Monte Carlo Samples and Triggers	36
6.1.2	Event Selection	38
6.1.3	LS-di-Tau Data-Driven QCD background prediction	40
6.2	Data Driven method validation	44
7	Results	46
7.1	Results	46

7.2	Final Yields for LS channel	47
7.3	Systematics	48
7.4	Limits	51
8	SUSY VBF Studies at 13 TeV	53
9	Conclusion	54
10	Appendix	55
10.1	Physic Object Reconstruction	55
10.1.1	Jet Reconstruction	55
10.1.1.1	b-Jet Tagging	56
10.1.2	Tau Reconstruction and Identification	56
10.2	Physic Object Reconstruction at 13 TeV	57

1 Introduction

2 Theory

2.1 The Standard Model of Particle Physics

	1st Generation	2 Generation	3rd Generation	charge
leptons	$\begin{pmatrix} \nu_e \\ e \end{pmatrix}_L$ e_R	$\begin{pmatrix} \nu_\mu \\ \mu \end{pmatrix}_L$ μ_R	$\begin{pmatrix} \nu_\tau \\ \tau \end{pmatrix}_L$ τ_R	weak weak, electromagnetic electromagnetic
leptons	$\begin{pmatrix} u \\ d \end{pmatrix}_L$ u_R, d_R	$\begin{pmatrix} c \\ s \end{pmatrix}_L$ c_R, s_R	$\begin{pmatrix} t \\ b \end{pmatrix}_L$ t_R, b_R	weak, electromagnetic, strong electromagnetic, strong

Figure 2.1: Fermions of the Standard Model and their charges, arranged in the three generations. Only the left-handed fermions interact weakly and are arranged in doublets. The right-handed fermions are singlets. The right-handed neutrinos are not present in this table, as they do not interact with one of the forces of the Standard Model.

Property/Interaction	Gravitation	Electroweak	Strong	
			Fundamental	Residual

Figure 2.2: The Standard Model classified all four fundamental forces in nature. In the Standard Model, a force is described as an exchange of bosons between the objects affected, such as a photon for the electromagnetic force and a gluon for the strong interaction. Those particles are called force carriers. [https : //en.wikipedia.org/wiki/Standard_Model](https://en.wikipedia.org/wiki/Standard_Model)

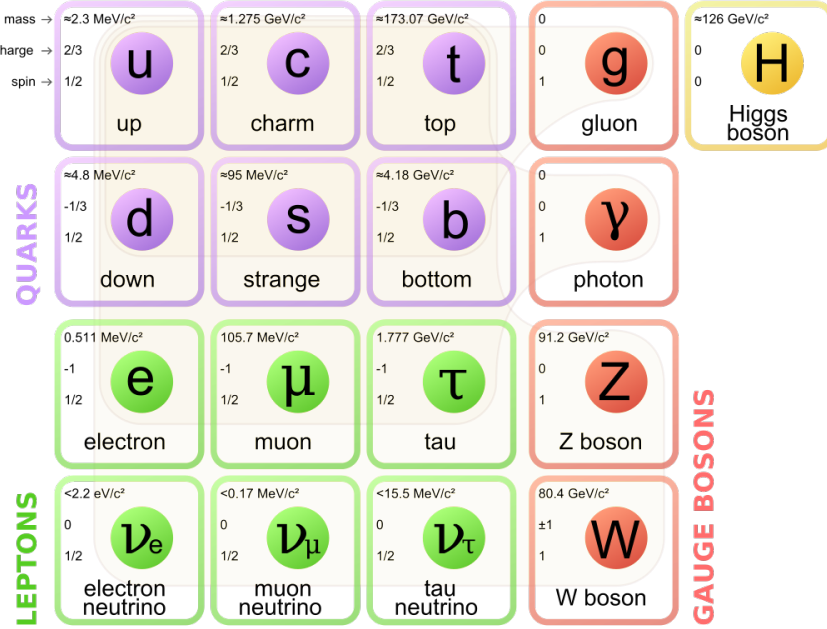


Figure 2.3: The Standard Model of elementary particles consists of 12 fundamental fermions and 4 fundamental bosons. Brown loops indicate which bosons (red) couple to which fermions (purple and green).

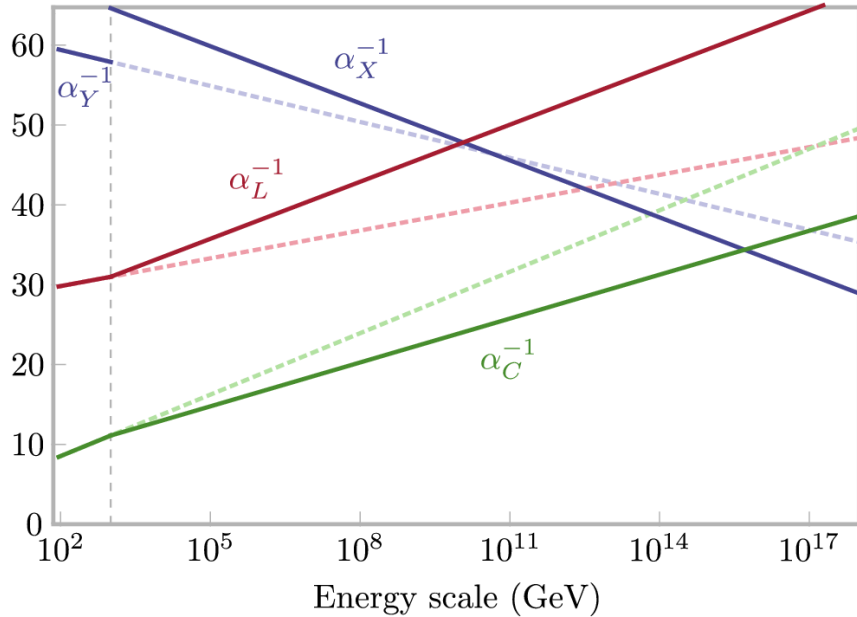


Figure 2.4: Running of the gauge coupling constants in the SM (dashed lines) and in the model in Ref. [?] (solid lines). Here the M_{331} scale is set to 11 TeV

2.2 Supersymmetry

Supersymmetry is one of the most intriguing and fundamental concepts in modern theoretical particle physics. It arises naturally from the combination of the two cornerstones of 20th century physics: quantum mechanics and relativity. Supersymmetry is the unique symmetry that relates the two fundamental kinds of particles: bosons, which act as the carriers of forces, and fermions, which act as the constituents of matter. Supersymmetry transformations are in a sense like the square roots of the coordinate system transformations in special relativity, and consequently supersymmetric quantum field theories have very special, improved properties, compared to ordinary relativistic quantum field theories. If supersymmetry is realized in nature, every fermion in the SM must have a bosonic partner particle and vice versa. No such superpartner particle has been observed so far but there are more and more indications that these particles might show up at the LHC experiments.

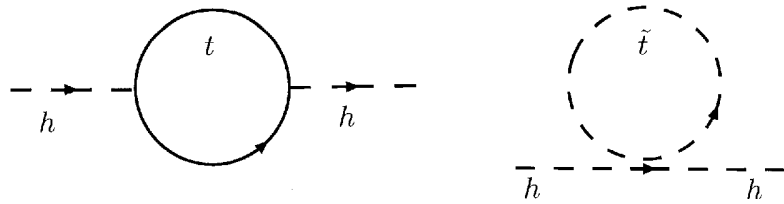


Figure 2.5: In SUSY, the correction to Higgs mass by the top quark (L) is inherently cancelled by the contribution from the top quark's supersymmetric partner, the stop (R).

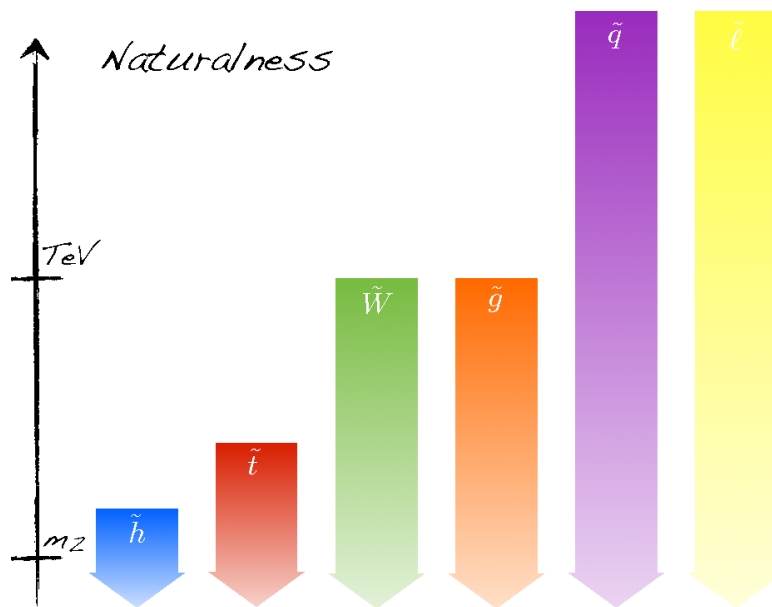
2.2.1 Motivations

2.2.2 The MSSM

2.2.3 SUSY Signatures at the LHC

Names	Spin	P_R	Gauge Eigenstates	Mass Eigenstates
Higgs bosons	0	+1	$H_u^0 \ H_d^0 \ H_u^+ \ H_d^-$	$h^0 \ H^0 \ A^0 \ H^\pm$
squarks	0	-1	$\tilde{u}_L \ \tilde{u}_R \ \tilde{d}_L \ \tilde{d}_R$ $\tilde{s}_L \ \tilde{s}_R \ \tilde{c}_L \ \tilde{c}_R$ $\tilde{t}_L \ \tilde{t}_R \ \tilde{b}_L \ \tilde{b}_R$	(same) (same) $\tilde{t}_1 \ \tilde{t}_2 \ \tilde{b}_1 \ \tilde{b}_2$
sleptons	0	-1	$\tilde{e}_L \ \tilde{e}_R \ \tilde{\nu}_e$ $\tilde{\mu}_L \ \tilde{\mu}_R \ \tilde{\nu}_\mu$ $\tilde{\tau}_L \ \tilde{\tau}_R \ \tilde{\nu}_\tau$	(same) (same) $\tilde{\tau}_1 \ \tilde{\tau}_2 \ \tilde{\nu}_\tau$
neutralinos	1/2	-1	$\tilde{B}^0 \ \tilde{W}^0 \ \tilde{H}_u^0 \ \tilde{H}_d^0$	$\tilde{N}_1 \ \tilde{N}_2 \ \tilde{N}_3 \ \tilde{N}_4$
charginos	1/2	-1	$\tilde{W}^\pm \ \tilde{H}_u^+ \ \tilde{H}_d^-$	$\tilde{C}_1^\pm \ \tilde{C}_2^\pm$
gluino	1/2	-1	\tilde{g}	(same)
goldstino (gravitino)	1/2 (3/2)	-1	\tilde{G}	(same)

Figure 2.6: SUSY particles in MSSM [?]

Figure 2.7: Cartoon illustration of the mass scales for various sparticles dictated solely by electroweak naturalness with sensitivity parameter $\Delta \lesssim 10$.

3 The Experimental Setup

3.1 The Large Hadron Collider

The Large Hadron Collider (LHC) is the world's largest and most powerful particle collider, the largest, most complex experimental facility ever built, and the largest single machine in the world.[1] It was built by the European Organization for Nuclear Research (CERN) between 1998 and 2008 in collaboration with over 10,000 scientists and engineers from over 100 countries, as well as hundreds of universities and laboratories. It lies in a tunnel 27 km in circumference, as deep as 175 m beneath the FranceSwitzerland border near Geneva, Switzerland, originally build for the Large Electron Positron Collider (LEP).

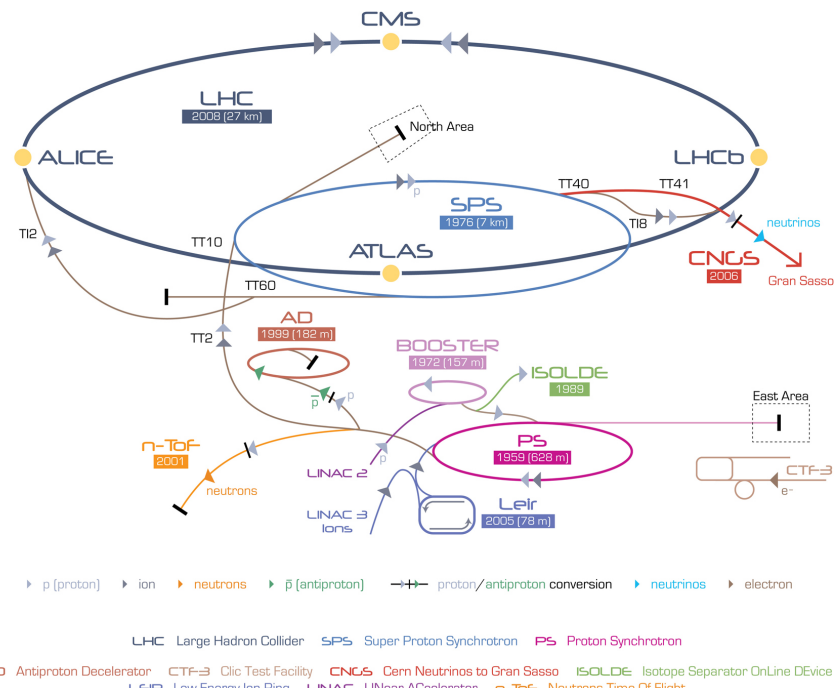


Figure 3.1: Schematic view of the LHC with its four big experiments. Also shown are the pre-accelerators, as well as several other experiments operated at CERN.

The Large Hadron Collider (LHC) is a proton-proton collider at the European Organization for Nuclear Research (CERN), residing in the 26.7 km tunnel originally build for the Large Electron Positron Collider (LEP). It consists of two rings with counter-rotating beams, being crossed at four interaction points. The proton beams are ramped up to the energy of 450 GeV by a chain of pre-accelerators, and are then injected into the LHC ring (Figure 3.1). LHC first official run started on March 2010 and last for almost 3 years with an initial energy per beam of 3.5 TeV (7 TeV in total), rising to 4 TeV per beam (8 TeV in total) in 2012. The shutdown in 2013 was followed by two years of technical upgrades

after that the LHC restarted the run with a total beam energy of 13 TeV. The design luminosity of L is $10^{34} \text{ cm}^{-2} \text{ s}^{-1}$ has been reached in june 2016, with a bunch crossing every 25ns . Figure 3.2 shows the total cross section prospects for LHC in comparison with several Standard Model processes. In 2012 LHC delivered a total luminosity of 23.30 fb^{-1} as shown on 3.3.

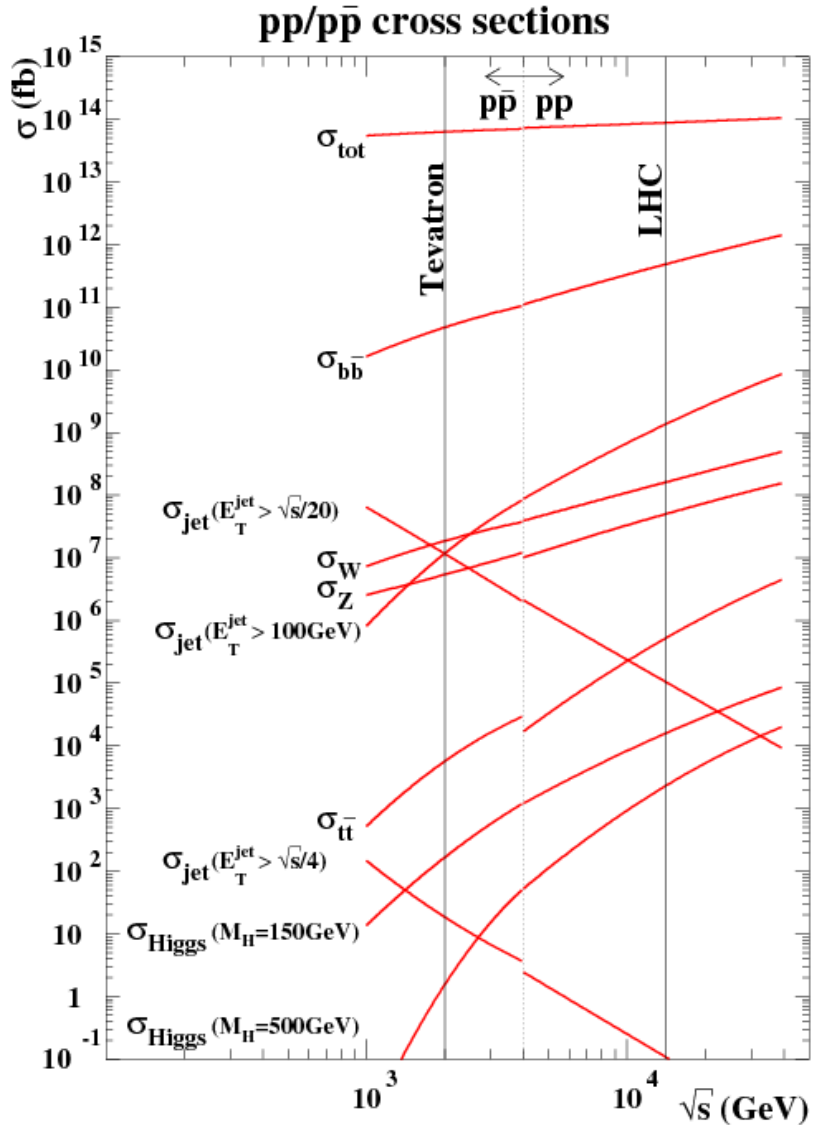


Figure 3.2: Production cross-sections for several representative processes at hadron colliders as a function of the machine center-of-mass energy

Several experiments are hosted at the LHC. ATLAS (A Toroidal Lhc ApparatuS) ?? and CMS (Compact Muon Solenoid) ?? are multi-purpose detectors, aiming at Standard Model physics including Higgs searches and physics beyond the Standard Model. LHCb ?? is dedicated to b-quark physics and the related problem of CP violation the matter-antimatter asymmetry in the universe. As the LHC can also be run in heavy ion (lead-lead) collision mode, one experiment, ALICE (A Large Ion Collider Experiment) ??, focuses on

strongly interacting matter and quark-gluon plasma. Finally, another two experiments, LHCf ?? and TOTEM (TOTal Elastic and diffractive cross section Measurement) ?? are designed to study the total proton-proton interaction cross-section. The site for each of the previously mentioned experiments is shown in Figure 3.1.

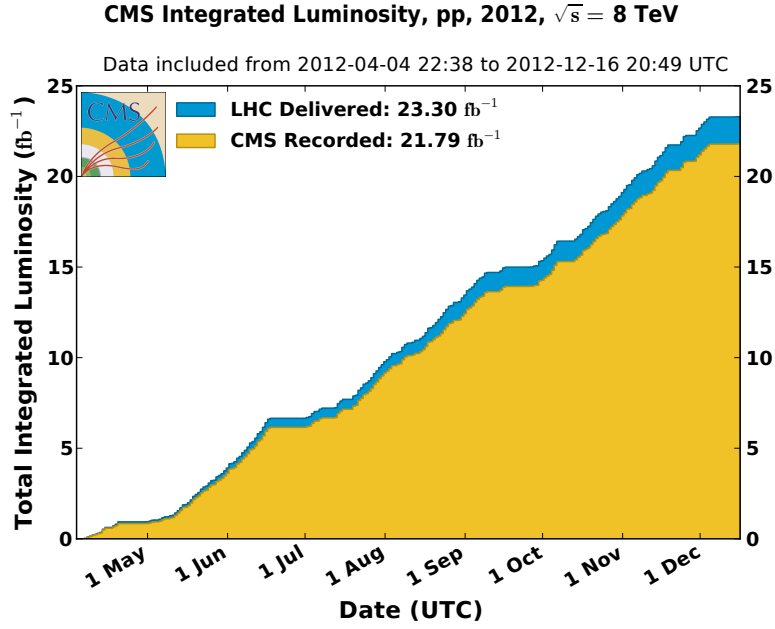


Figure 3.3: Cumulative luminosity versus day delivered to (blue), and recorded by CMS (orange) during stable beams and for p-p collisions at 8 TeV centre-of-mass energy in 2012. The delivered luminosity accounts for the luminosity delivered from the start of stable beams until the LHC requests CMS to turn off the sensitive detectors to allow a beam dump or beam studies. Given is the luminosity as determined from counting rates measured by the luminosity detectors. These detectors have been calibrated with the use of the van-der-Meer beam-separation method, where the two beams are scanned against each other in the horizontal and vertical planes to measure their overlap function.

3.2 The CMS Experiment

The Compact Muon Solenoid is a "general purpose" experiment placed at Point 5 along the LHC ring. The experiment has a cylindrical geometry and is divided in two main sections: the lateral section, called Barrel and the remaining ones called Endcaps (Figure 3.4). CMS was designed to fulfill the following important research tasks:

1. Search for the Higgs Boson
2. Search for physics beyond the standard model

those tasks combined with the LHC design specifications require a detector with the following characteristics:

- High granularity and response;
- High radiation damage resistance;
- Good performances in the reconstruction of the μ particle charge, momentum and invariant mass;
- Good τ particle and jets reconstruction efficiency;
- High resolution on the combined reconstruction of electrons and photons;
- Great phase-space coverage $|\eta| < 5$;
- Good resolution in the missing transverse energy reconstruction.

The CMS detector has a $24m$ length and a $14.6m$ diameter for a total weight of $14500t$. The experiment is made of several sub-detectors placed concentrically around the interaction point, each one providing complementary measurements (Figure 3.5). Particles coming from the interaction point first go through the tracking system which measures the position of charged particles hitting its layers. The calorimeters are placed right outside the tracking system and are capable of measuring the particles energy deposits. The Electromagnetic Calorimeter (ECAL) measures the energy of electrons and photons, the Hadronic Calorimeter (HCAL) measures the energy of all fermions containing quarks.

The most important section in the detector is the high magnetic field which allows the measurement of high momentum charged particles with high precision. Measurements with high resolution standards require high magnetic fields, therefore the choice to use superconducting technology for the magnets. All previously introduced sub-detectors are contained inside the solenoid superconducting magnet. All particles except for μ and low interacting ones get contained by the calorimeters and the magnetic return yoke. Outside the magnet there are the muon chambers which identify μ particles and measure their momentum.

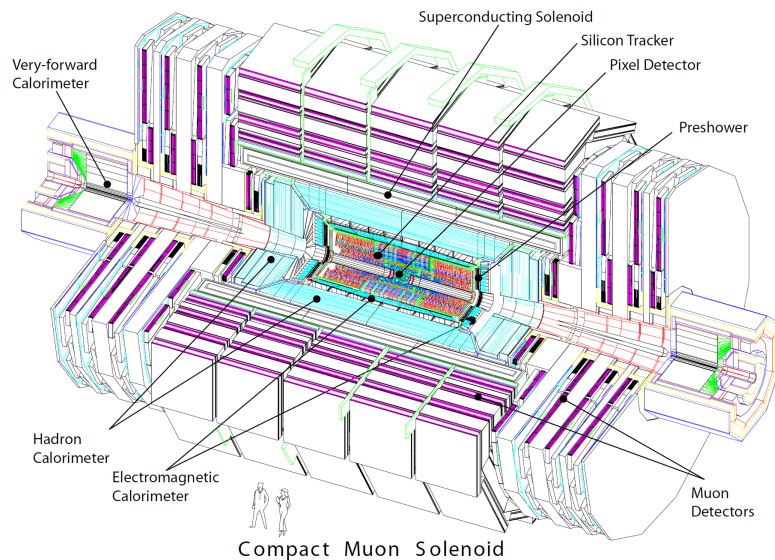


Figure 3.4: An exploded view of the CMS detector.

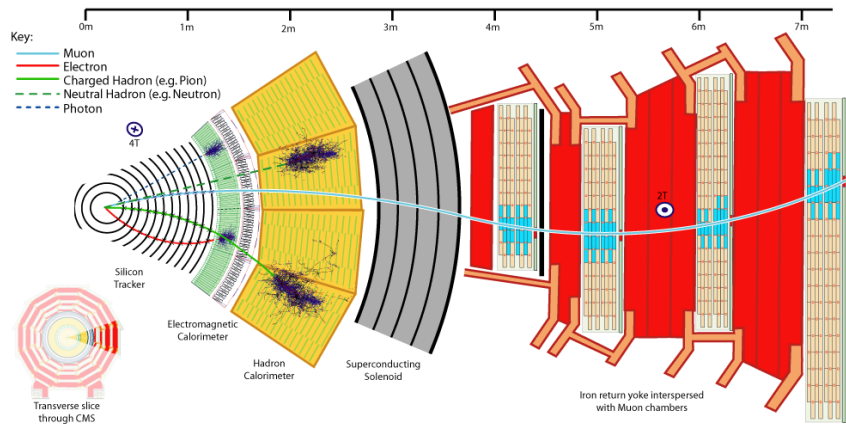


Figure 3.5: Longitudinal section of the CMS detector showing the different detectors components and position.

3.2.1 The Magnet

The precision requirements of the muon chambers in order to distinguish unambiguously $\approx 1 \text{ TeV}/c$ muon charge is $\Delta p/p \approx 10\%$ therefore the requirement of a magnetic field with high bending power. The main features of the CMS solenoid are the use of a high-purity aluminium-stabilised conductor and indirect cooling (by thermosyphon), together with full epoxy impregnation.

The CMS magnet is large superconducting solenoid with an inner bore of 5.9 m and a length of 12.9 m. This good length/radius ratio is necessary to ensure good momentum resolution in the forward region as well. Its size is enough to contain the tracking system, the electromagnetic calorimeter and the hadronic calorimeter.

The high magnetic field of 4 T is generated by a current of 19,5 kA going through 2168 coil turns. An important parameter for this superconducting magnets design is the value of the hoop stress of 64 atm produced by the magnetic pressure due to the Lorentz force. The amount of total energy stored by the superconducting magnet is of 2.7 GJ.

3.2.2 Inner tracking system

The Inner Tracking systems reconstructs the track of charged particles and measures their momentum. In order to meet the design requirements of a compact design and high reconstruction efficiency (95% for high momentum μ particles) the main detector material is silicon. The detector can be easily divided in three parts:

- Placed close to the interaction point where the particle flux is higher are the pixel detectors. Each pixel is $100 \times 150 \mu\text{m}^2$ wide;
- In the intermediate region ($20 < r < 55\text{cm}$) the particle flux is low enough to allow the usage of silicon micro-strips, with each cells with the minimum size of $10\text{cm} \times 80\mu\text{m}$;
- in the outermost region ($r > 55\text{cm}$), the particle flux is low enough to allow bigger size micro-strips with size of $25\text{cm} \times 180\mu\text{m}$

A section of the whole Inner Tracking apparatus on the z-plane is viewable in Figure 3.6. Close to the interaction point 3 pixel-layers are placed at radial distances of 4.7, 7.3 and 10.2cm . In the Barrel region the silicon micro-strips are placed at a radial distance between 20 and 110cm . The forward region has instead 2 pixel and 9 micro-strips layers. The barrel micro-strip section is divided in 2 different parts: the innermost and the outermost one. In order to avoid excessively shallow track crossing angles, the Inner Barrel region is shorter than the Outer one, and there are an additional 3 Inner Disks in the transition region between the Barrel and Endcap parts, on each side of the Inner Barrel. The overall inner layout apparatus is viewable in Figure 3.7. The total area of the pixel detector is $\approx 1\text{m}^2$, whilst that of the silicon strip detectors is 200m^2 , providing coverage up to $|\eta| < 2.4$. The inner tracker comprises 66 million pixels and 9.6 million silicon strips. The silicon pixels grants a precision of $10\mu\text{m}$ on the (x, y) transverse plane and of $20\mu\text{m}$ on the z axis. The resolution of the silicon micro-strips depends on each cell thickness, with a minimum value of $55\mu\text{m}$ for the traverse plane.

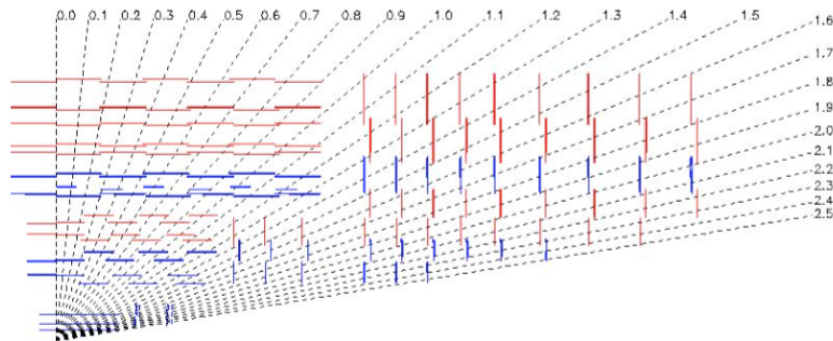


Figure 3.6: The tracker layout (1/4 of the z view).

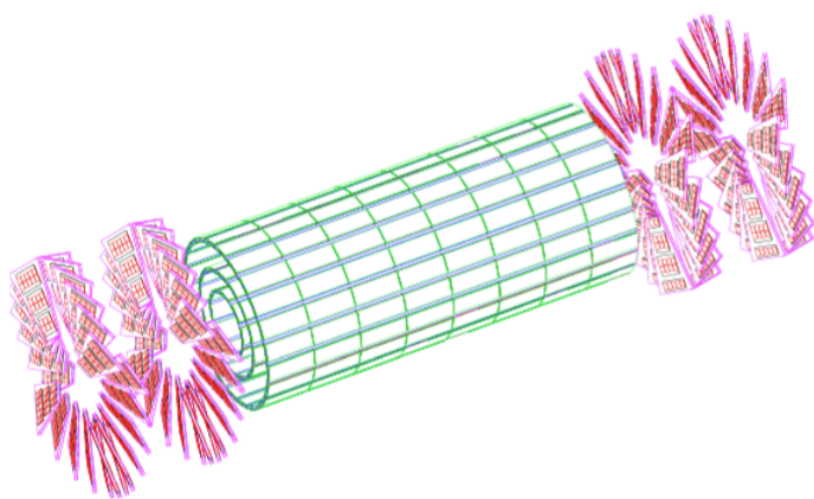


Figure 3.7: Layout of pixel detectors in the CMS tracker.

3.2.3 The Electromagnetic calorimeter

The Electromagnetic Calorimeter (ECAL) is a hermetic, homogeneous calorimeter comprising 61200 lead tungstate ($PbWO_4$) crystals mounted in the central barrel part, closed by 7324 crystals in each of the 2 endcaps. The crystal material choice was driven by the short radiation length and Molire ray, granting compactness and good granularity as listed on Table 3.8. Other $PbWO_4$ important properties are radiation resistance and the short decaying time which allows to collect the 85% of light during the 25 ns interval between a bunch crossing and the next one.

Density	$8.28 g/cm^3$
X_0	$0.89 cm$
R_M	$2.2 cm$

Figure 3.8: Parameters of the $PbWO_4$ crystals .

The Ecal is made of a central body in the Barrel region and two identical structures covering the Endcap ones. The final design aim was to build a calorimeter as compact as possible. In order to have high hermeticity the space in between crystals has been reduced as much as possible especially in the transition region between Barrel and Endcaps.

The Barrel covers a pseudo-rapidity region of $|\eta| < 1.479$ with its cylinder ray of 129 cm. It contains 61200 crystals; 360 placed in ϕ and 2×85 in η . The crystals are quasi-projective (the axes are tilted at 3° with respect to the line from the nominal vertex position) and cover 0.0174 (i.e. 1°) in $\Delta\phi$ and $\Delta\eta$. The crystals have a front face cross-section of $\approx 22 \times 22 mm^2$ and a length of 230 mm, corresponding to $25.8X_0$. The Endcaps cover the pseudo-rapidity of $1.48 < |\eta| < 2.6$ where the $2.6 \times 2.6 \times 22 cm^3$ are gathered in 5×5 matrices called supercrystals.

In the pseudo-rapidity interval of $1.653 < |\eta| < 2.56$, as shown on Figure 3.9, is present a detector called Preshower, halo-ring shaped. The preshower is a sampling calorimeter made by two distinct layers; the showering layer made of lead and the detector layer made of silicon strips capable of measuring the energy deposit of the initial part of particle showers as well as their lateral profile. The role of this detector is important whenever multiple particle showers overlap in the ECAL Endcap allowing a clear distinction of each of those showers.

The overall ECAL resolution can be parametrized as a function of the energy measured:

$$\frac{\sigma}{E} = \frac{S}{\sqrt{E}} + \frac{N}{E} + C^2 \quad (3.1)$$

where S is the stochastic term, N the noise and C the constant term. The values of these parameters are listed on Figure 3.10.

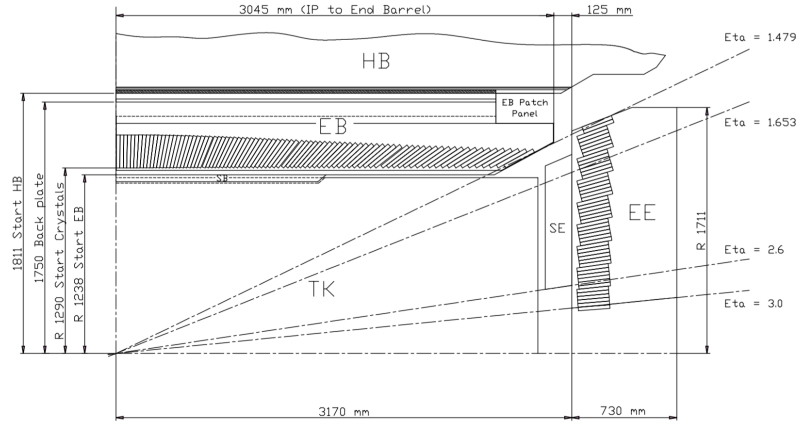


Figure 3.9: Longitudinal section of the electromagnetic calorimeter (one quadrant).

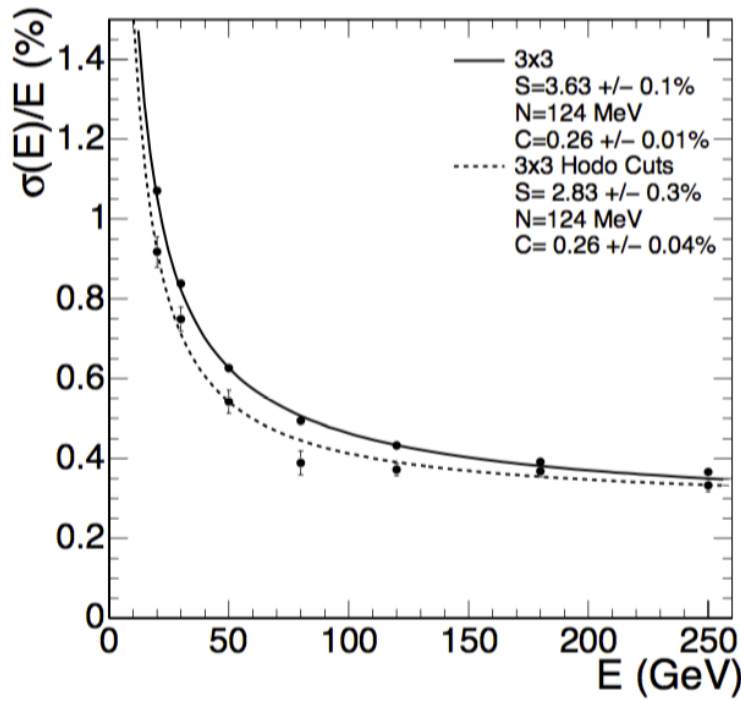


Figure 3.10: ECAL supermodule energy resolution, σ_E/E , as a function of electron energy as measured from a beam test. The upper series of points correspond to events taken with a $20 \times 20 \text{ mm}^2$ trigger and. The lower series of points correspond to events selected to fall within a $4 \times 4 \text{ mm}^2$ region. The energy was measured in an array of 3×3 crystals with electrons impacting the central crystal.

3.2.4 The Hadron calorimeter

The Hadronic Calorimeter (HCAL) is used along side with the electromagnetic one in order to measure the energy deposit and position in the detector for hadronic jets, the transverse energy and the missing transverse energy \cancel{E}_T . The requirements for this detector are to minimize as much as possible the Gaussian tail of the resolution distribution and good containment of the hadronic showers in order to have good \cancel{E}_T measurements. Its design is influenced by the choice of the magnet parameters since it is located inside the superconducting magnet along with the ECAL and the inner tracking system.

The hadron Barrel (HB) part of HCAL consists of 32 towers covering the pseudo-rapidity region $1.4 < \eta < 1.4$, resulting in 2304 towers with a segmentation $\Delta\eta \times \Delta\phi = 0.087 \times 0.087$, corresponding to a 5×5 ECAL crystal tower. The HB is constructed in 2 half barrels. The HB is readout as a single longitudinal sampling. There are 15 brass plates, each with a thickness of about 5 cm, plus 2 external stainless steel plates for mechanical strength. Particles leaving the ECAL volume first see a scintillator plate with a thickness of 9 mm rather than 3.7 mm for the other plates. The light collected by the first layer is optimized to be a factor of about 1.5 higher than the other scintillator plates. The radiation length λ_0 for HB is 8.9.

Each hadron Endcap (HE) of HCAL consists of 14 η towers with $5^\circ \phi$ segmentation, covering the pseudo-rapidity region $1.3 < |\eta| < 3.0$. For the 5 outermost towers (at smaller η) the ϕ segmentation is 5° and the η segmentation is 0.087. For the 8 innermost towers the ϕ segmentation is 10° , whilst the η segmentation varies from 0.09 to 0.35 at the highest η . The total number of HE towers is 2304. The radiation length λ_0 for HE is 10.0.

In order to improve the shower containment there's another calorimeter, called "Tail catcher" placed right outside the magnet. As further hermeticity improvement a "forward" calorimeter (HF) has been installed at around 11 meters from the interaction point, covering the η region of $3.0 < |\eta| < 5.0$. This calorimeter is made of steel/quartz fibres running parallel to the beam line.

Figure 3.11 shows the longitudinal section of the HCAL and the locations of its parts HB, HE, HF and HO.

The HCAL energy resolution is:

$$\frac{\sigma(E)}{E} = \frac{100\%}{\sqrt{E}} \oplus 4.5\% \quad (3.2)$$

Table 3.12 shows the distribution of the jet energy resolution as function of the simulated jet traverse energy.

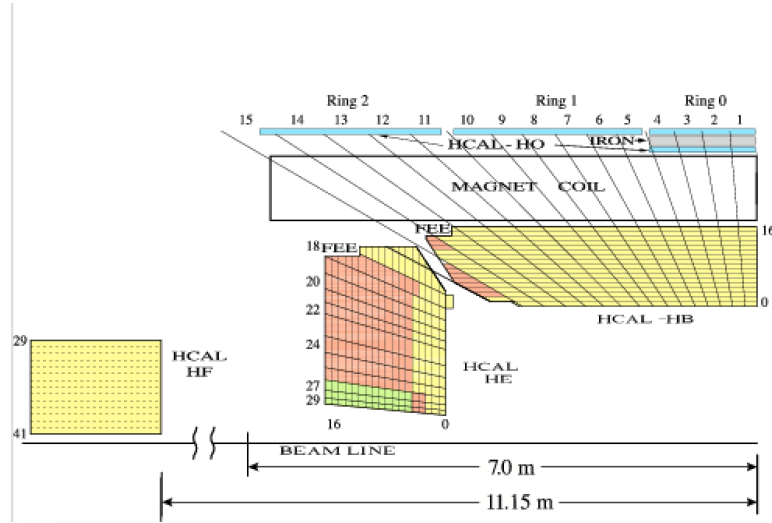


Figure 3.11: The CMS HCAL detector (quarter slice). "FEE" indicates the locations of the Front End Electronics for HB and HE. The signals of the tower segments with the same color are added optically, to provide the HCAL "longitudinal" segmentation. HB, HE and HF are built of 36 identical azimuthal wedges ($\Delta\phi = 20$ degrees).

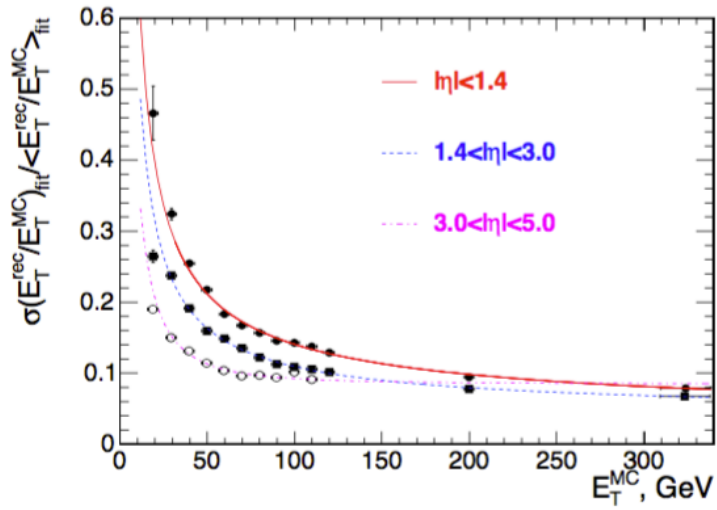


Figure 3.12: The jet transverse energy resolution as a function of the simulated jet transverse energy for barrel jets ($|\eta| < 1.4$), endcap jets ($1.4 < |\eta| < 3.0$) and very forward jets ($3.0 < |\eta| < 5.0$). The jets are reconstructed with the interative cone $R = 0.5$ algorithm.

3.2.5 The Muon System

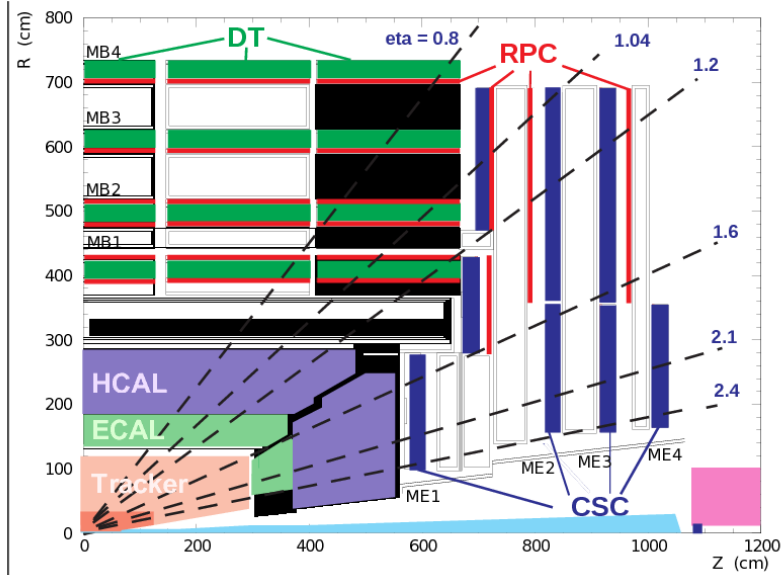


Figure 3.13: Layout of one quarter of the CMS muon system for initial low luminosity running. The RPC system is limited to $|\eta| < 1.6$ in the endcap, and for the CSC system only the inner ring of the ME4 chambers have been deployed.

Three types of gaseous detectors are used to identify and measure muons ???. The choice of the detector technologies has been driven by two reasons: the high radiation environment and the large surface to cover. Since in the barrel region of $|\eta| < 1.2$, both the muon rate and the residual magnetic field in the chambers is low, drift tube (DT) chambers are used. In the 2 endcaps instead, where the muon rate as well as the neutron induced background rate is high, and the magnetic field is also high, cathode strip chambers (CSC) are placed covering the pseudo-rapidity region up to $|\eta| < 2.4$. Additionally, resistive plate chambers (RPC) are used in both the barrel and the endcap regions covering a pseudo-rapidity region of $|\eta| < 2.1$. These RPCs operate in avalanche mode to ensure good performances at high rates and have double gaps with a gas gap of 2 mm. RPCs provide a fast response with good time resolution but with a coarser position resolution than the DTs or CSCs. RPCs can therefore identify unambiguously the correct bunch crossing.

The DTs or CSCs and the RPCs operate within the first level trigger system, providing independent and complementary sources of information. The layout of one quarter of the CMS muon system for initial low luminosity running is shown in Figure 3.13. In total, the muon system contains of order 25000 m^2 of active detection planes, and nearly 1 million electronic channels.

3.2.6 The Trigger System

With a bunch crossing rate of 40 Mhz at design luminosity and the possibility to record the information for $\approx 10^2$ crossings/sec the CMS experiment needs a trigger system capable of a rejeftion factor of at least 10^6 .

The CMS trigger and data acquisition system (DAQ) consist of 4 parts: the detector electronics, the hardware-based level 1 trigger, the readout network and and the online event filter system that uses a software-based high level trigger (HLT).

There's a minimum transit time required for the signal to reach the level one trigger hardware based on the service tunnels next to the CMS experiment site, wait for the trigger response to keep or discard the event and send it back to the detectors readout apparatus. The average time needed for a single cycle is $3.2 \mu s$. During the following time the event information is stored in a buffer waiting for the Level-1 trigger response. The trigger decisional time is less than $1 \mu s$ with a rejection power of around 1 crossing kept every 1000.

The Level-1 decision is based on "trigger primitive" objects such as photons, electrons and muons and jets above thresholds as well as the transverse energy E_T and the missing transverse energy \cancel{E}_T involving the calorimetry and the muon system and a combination between these detectors. Since the Level-1 trigger is meant to take fast decisions at a high rate (the design value is 100kHz) the trigger objects are reconstructed with reduced resolution and granularity. A safe time margin of a factor of 3 is taken into account in order to cover for possible reconstruction uncertainties as well as beam and detector conditions leading to a rate of 16kHz. The design value of 100 kHz is set by the average time to transfer full detector information through the readout system. A schematic overview of the Level-1 Trigger structure is shown on figure ??.

Once an event passes the Level-1 trigger selection the data from the pipelines to the front end readout buffers waiting for a further event reconstruction. After a successful reconstruction the compressed event is sent to one processors of the available farm that runs the same High Level Trigger (HLT) software. The main aim of the HLT is to gather all the informations collected in the event in order to trigger over more complex objects such as τ particles, multiple jets and multiple particle object or event reconstructed quantities in order to further reduce the event rate from 100kHz to 100Hz for mass storage.

3.2.7 Software and Computing

The CMS software and computing systems covers a broad range of tasks:

- online and offline calibration and status reports for each of the subdetectors;
- management, maintenance and access of the data storage;
- reconstruction and analysis of data;
- support of the distributed computing infrastructure and software framework.

The scale of the CMS collaboration in terms of storage capabilities, networking power is orders of magnitude higher than the CERN’s infrastructure capabilities. Therefore the CMS computing model is highly distributed, with a primary ”Tier-0” centered at CERN with the additional support by ”Tier-1” and ”Tier-2” computing centers scattered worldwide in several universities and research centers.

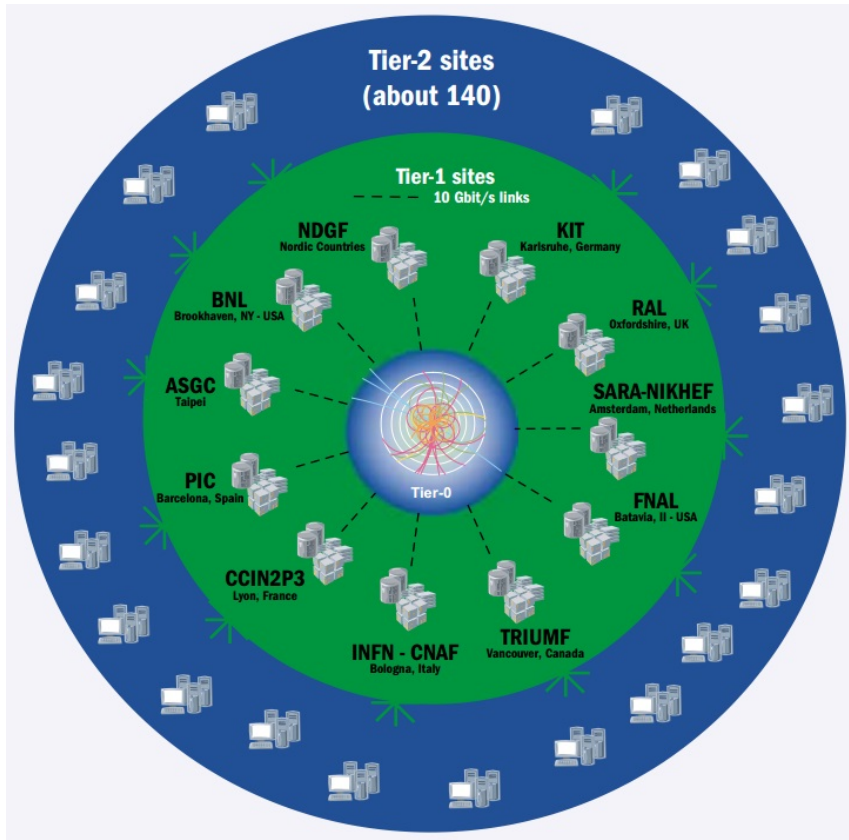


Figure 3.14: Overview of the structure of the CMS Computing Grid.

The scale of the CMS collaboration in terms of storage capabilities, networking power is orders of magnitude higher than the CERN’s infrastructure capabilities. Therefore the CMS computing model is highly distributed consisting of four layers, or ”tiers”; 0, 1, 2 and 3. Each tier provides a specific set of services.

All those facilities as shown on Figure 3.14 have hierarchical structure under the Tier-0 and go under the name of ”CMS Computing Grid”.

3.2.7.1 Tier-0

This is the CERN Data Centre, which is located in Geneva, Switzerland and also at the Wigner Research Centre for Physics in Budapest, Hungary over 1200km away. The two sites are connected by two dedicated 100 Gbit/s data links. All data from the LHC passes through the central CERN hub, but CERN provides less than 20% of the total compute capacity.

Tier 0 is responsible for the safe-keeping of the raw data (first copy), first pass reconstruction, distribution of raw data and reconstruction output to the Tier 1s, and reprocessing of data during LHC down-times.

3.2.7.2 Tier 1

These are thirteen large computer centres with sufficient storage capacity and with round-the-clock support for the Grid. They are responsible for the safe-keeping of a proportional share of raw and reconstructed data, large-scale reprocessing and safe-keeping of corresponding output, distribution of data to Tier 2s and safe-keeping of a share of simulated data produced at these Tier 2s.

3.2.7.3 Tier 2

The Tier 2s are typically universities and other scientific institutes, which can store sufficient data and provide adequate computing power for specific analysis tasks. They handle analysis requirements and proportional share of simulated event production and reconstruction.

There are currently around 160 Tier 2 sites covering most of the globe.

3.2.7.4 Tier 3

Individual scientists will access these facilities through local (also sometimes referred to as Tier 3) computing resources, which can consist of local clusters in a University Department or even just an individual PC. There is no formal engagement between WLCG and Tier 3 resources.

4 Search for SUSY in Vector Boson Fusion Processes at the LHC

4.1 Introduction

Many of the searches for $\tilde{\chi}_1^\pm$ and $\tilde{\chi}_2^0$ in ATLAS and CMS involves the search for signal events with 3 leptons and \cancel{E}_T . On the other hand there are very few searches involving final states with τ leptons due to the larger τ misidentification rate which makes harder to keep the background under control as well as having low p_T thresholds for triggering.

There is however the possibility to study final states with 2τ and \cancel{E}_T coming from the decay of $\tilde{\chi}_1^\pm$ and $\tilde{\chi}_2^0$ produced by Vector Boson Fusion (VBF) processes. This search comes with some important advantages.

Firstly with the increasing LHC luminosity both ATLAS and CMS needs to raise the p_T thresholds on the triggered objects. Is it possible however to probe signal for SUSY in VBF events by triggering over the VBF properties of the event, leaving the decay products of $\tilde{\chi}_1^\pm$ and $\tilde{\chi}_2^0$ free from trigger bias.

Secondly scenarios involving the naturalness of SUSY allows $\tilde{\tau}_1$ lighter than $\tilde{\mu}_1$ and \tilde{e}_1 for high values of $\tan \beta$. A light $\tilde{\tau}_1$ with small mass splitting also is favored in coannihilation processes ?? that set the relic density to correct values, in the case of Bino dark matter. Light $\tilde{\tau}_1$ is also motivated in the context of the MSSM by the enhancement of the $H \rightarrow \gamma\gamma$ channel ?? . All of these facts stress on the importance of the search for low $p_T \tau$ final states with large background contribution, for which production by the VBF processes since is possible to take advantage of its signature in order to reduce the background contribution to acceptable levels.

As third and final reason a VBF based search can be complementary to the existing one at LHC based on Drell-Yan production since is not constrained by any trigger bias.

The Feynman diagrams for the typical $\tilde{\chi}_1^\pm \tilde{\chi}_2^0$ pair production are shown on Figure 4.1. The $\tilde{\chi}_1^\pm$ and $\tilde{\chi}_2^0$ coming from the VBF processes decays into the multiple leptons and $\tilde{\chi}_1^0$ final state with the following decay process for $\tilde{\chi}_1^\pm$

$$\tilde{\chi}_1^\pm \rightarrow \tilde{\tau}_1 \nu \rightarrow \tilde{\chi}_1^0 \tau \nu \quad (4.1)$$

and similarly for $\tilde{\chi}_2^0$

$$\tilde{\chi}_2^0 \rightarrow \tilde{\tau}_1 \tau \rightarrow \tilde{\chi}_1^0 \tau \tau \quad (4.2)$$

4.2 Search Strategy

For this type of search several benchmark points are defined under the following constraints:

- The $\tilde{\chi}_1^\pm$ and $\tilde{\chi}_2^0$ are mainly Wino, the $\tilde{\chi}_1^0$ is mainly Bino;

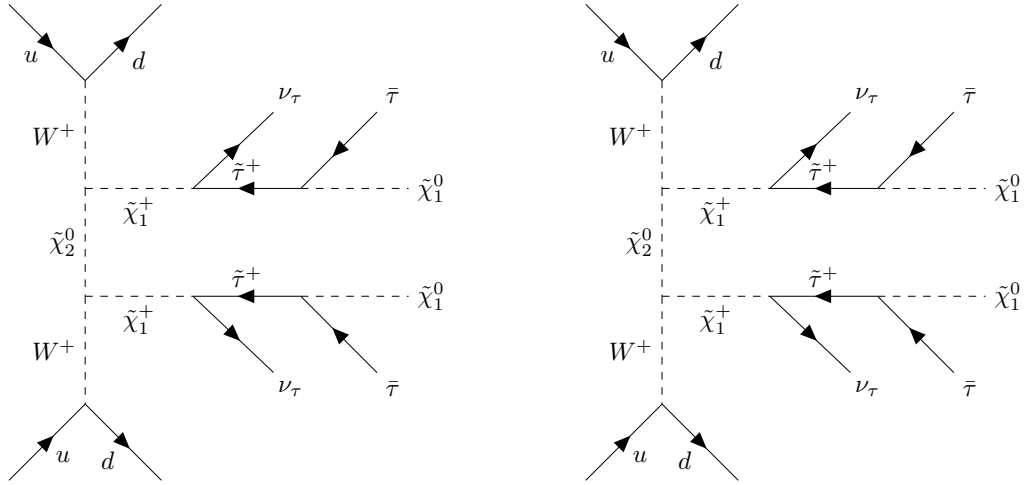


Figure 4.1: Diagrams of (left) $\tilde{\chi}_1^\pm \tilde{\chi}_2^0$ and (right) $\tilde{\chi}_1^\pm \tilde{\chi}_1^\mp$ pair production through vector-boson fusion followed by their decays to τ leptons and the LSP.

- The $\tilde{\chi}_1^\mp$ mass similar to the $\tilde{\chi}_2^0$ mass ($m_{\tilde{\chi}_1^\pm} \sim m_{\tilde{\chi}_2^0}$) and with values of 100, 200 and 300 GeV;
- The mass gap between the $\tilde{\tau}_1$ and $\tilde{\chi}_1^\pm$ is either 5 GeV or $(m_{\tilde{\tau}_1} - m_{\tilde{\chi}_1^\pm})/2$;
- The LSP mass is either $\tilde{\chi}_1^0 = 0, 50$ GeV;

The processes taken into account are

$$pp \rightarrow \tilde{\chi}_1^\pm \tilde{\chi}_1^\mp jj, \quad pp \rightarrow \tilde{\chi}_1^\pm \tilde{\chi}_2^0 jj, \quad pp \rightarrow \tilde{\chi}_2^0 \tilde{\chi}_2^0 \quad (4.3)$$

The cross-section prediction for those processes are summarized in Figure 4.2 as function of the $\tilde{\chi}_1^\mp$ - $\tilde{\chi}_2^0$ mass.

The search strategy can be divided in 2 distinct parts: the first one considers the kinematic of the jets produced via VBF in order to reduce the contribution coming from $V +$ jets events (where V is ether the W or Z boson); the second one takes into account the properties of the supersymmetric particles falling into the inner region of the detector (centrally produced) in order to reduce the all the non-supersymmetric background contributions.

The main feature of VBF processes is the production of two jets aimed at the forward-backward region of the detector with high p_T and large $\Delta\eta$. By adding in the event selection the requirements on the di-jet $\Delta\eta$ as well as the di-jet invariant mass $m_{j_1 j_2}$ the background contribution coming from $V +$ jets and $t\bar{t}$ events is kept under control. In order to generate super-symmetric particles, the incoming partons need to have an high momentum, therefore the leading jet from the VBF-produced di-jet pair is expected to have high p_T . The addition of a p_T cut on leading jets keeps further reduces background contributions. Figure 4.3 shows an early study on $m_{j_1 j_2}$ and leading jet p_T distributions for for $\tilde{\chi}_1^\pm \tilde{\chi}_1^\pm$ pair production by VBF processes, $V +$ jets background, and VV background produced by VBF processes.

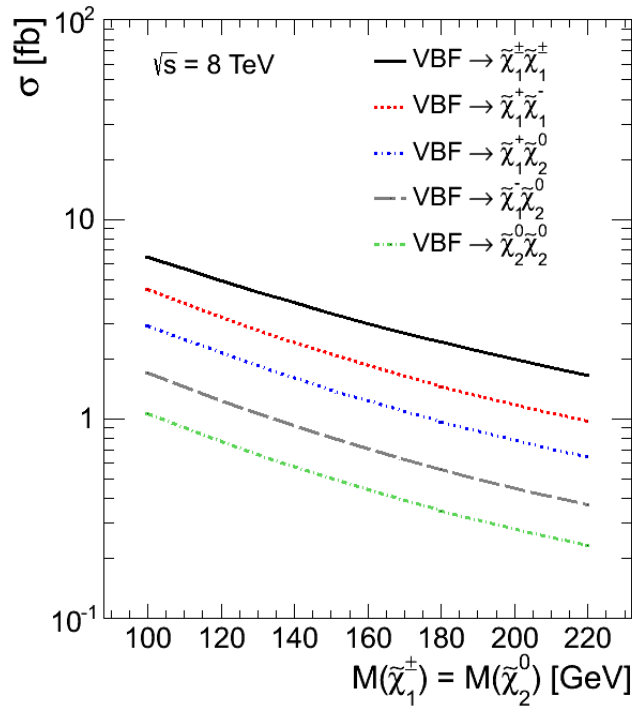


Figure 4.2: VBF production cross-section at $\sqrt{s}= 8$ TeV as a function of mass for various channels after imposing $\Delta\eta > 4.2$ using Madgraph 4.

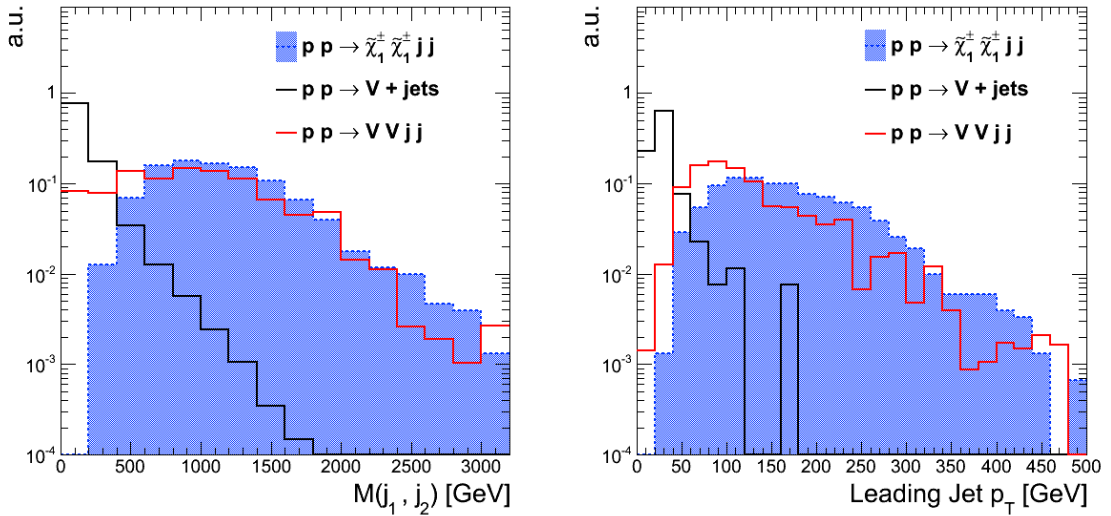


Figure 4.3: $m_{j_1 j_2}$ (left) and p_T of the leading jet (right) distributions normalized to arbitrary units for $\tilde{\chi}_1^\pm \tilde{\chi}_1^\pm$ pair production by VBF processes, V+jets background, and VV background produced by VBF processes.

The remaining background contributions come from all the centrally produced particles. By considering an R-parity conserving model the decay of $\tilde{\chi}_1^\pm$ and $\tilde{\chi}_2^0$ is the following

$$\tilde{\chi}_1^\pm \rightarrow \tilde{\tau}_1^\pm \nu \rightarrow \tau^\pm \tilde{\chi}_1^0 \nu \quad (4.4)$$

$$\tilde{\chi}_2^0 \rightarrow \tilde{\tau}_1^\pm \tau^\mp \rightarrow \tau^\pm \tau^\mp \tilde{\chi}_1^0 \quad (4.5)$$

The $\tilde{\chi}_1^0$ LSP travels through the detector undetected increasing \cancel{E}_T . The processes that mimics signal are all the VV (where V may be either W or Z) pairs produced via VBF where the bosons decays leptonically. A \cancel{E}_T cut is effective in reducing this background as shown on Figure 4.4. Moreover, requiring multiple τ s in the event further reduces background. The p_T of the τ coming from the $\tilde{\chi}_1^\pm$ and $\tilde{\chi}_2^0$ decays is strongly correlated to the mass difference between the $\tilde{\chi}_1^\pm$ and the $\tilde{\chi}_1^0$ LSP. In Figure 4.4, the normalized distribution of the p_T of τ is displayed for $\Delta M = m_{\tilde{\chi}_1^\pm} - m_{\tilde{\chi}_1^0} = 30 GeV and 15 GeV. For smaller ΔM , the distribution peaks at lower p_T and the signal acceptance is less efficient.$

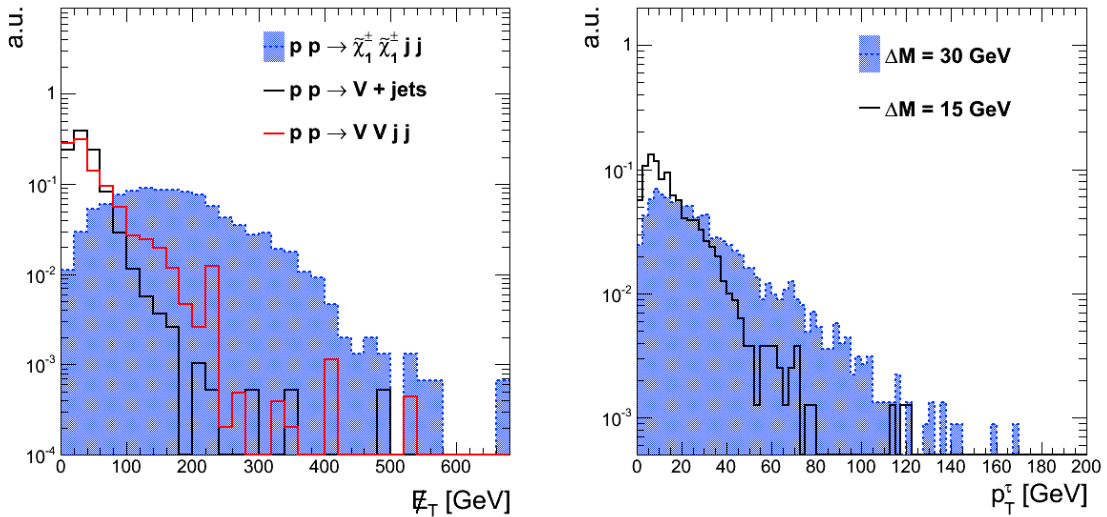


Figure 4.4: (left) \cancel{E}_T distribution normalized to arbitrary units for $\tilde{\chi}_1^\pm \tilde{\chi}_1^\pm$ pair production by VBF processes, V+jets background, and VV background produced by VBF processes. (right) p_T of τ distribution normalized to arbitrary units in $\geq 2j + 2\tau$ final state for $\Delta M = m_{\tilde{\chi}_1^\pm} - m_{\tilde{\chi}_1^0} = 30 GeV and 15 GeV.$

5 Objects Reconstruction

5.1 The Particle Flow Algorithm

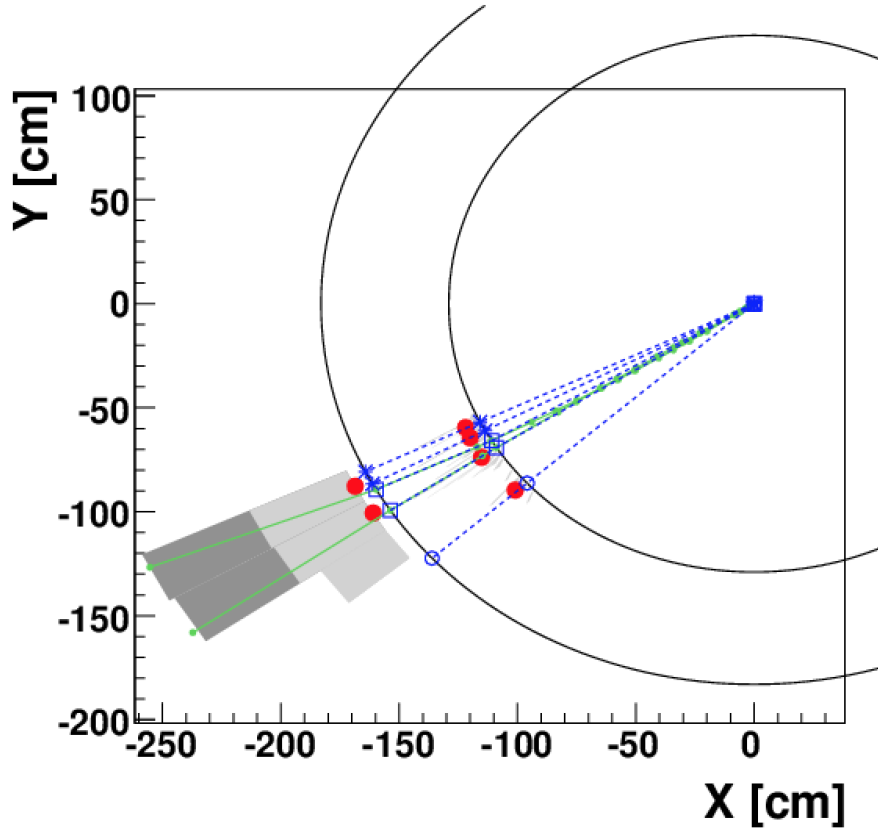
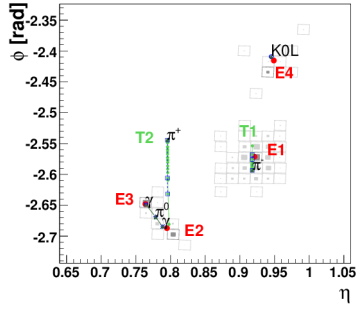
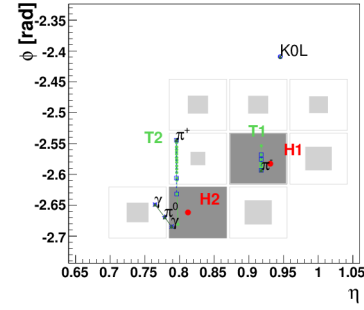
(a) The (x, y) view.(b) The (η, ϕ) view on ECAL.(c) The (η, ϕ) view on HCAL.

Figure 5.1: An event display of a simple hadronic jet in the (x, y) view (Figure 5.1a) and in the (η, ϕ) view, where η stands for pseudo-rapidity and ϕ for the azimuthal angle, on the ECAL surface (Figure 5.1b) and the HCAL surface (Figure 5.1c). (These two surfaces are represented as two circles centred around the interaction point in the first view.) The K_L^0 , the π^- and the two photons from the π^0 decay are detected as four well separated ECAL clusters (Figure 5.1b). The π^+ leaves no energy in the ECAL. The two charged pions are reconstructed as charged-particle tracks, appearing as vertical solid lines in the (η, ϕ) views and circular arcs in the (x, y) view. These tracks point towards two HCAL clusters (Figure 5.1c). In all three views, the cluster positions are represented by dots, the simulated particles by dashed lines, and the position of their impact on the calorimeter surfaces by various open markers.

5.2 The Tau Lepton reconstruction

With a lifetime of 2.9×10^{13} s and a mass of 1776.82 MeV the τ is the heaviest of the leptons. It was discovered between 1974 and 1977 by the team under Martin Perl while studying the $e^+ + e^- \rightarrow e^\pm + \mu^\mp$. The τ decays leptonically, with a branching ratio of 17% for each channel, via the following decay $\tau \rightarrow \nu_\tau W^* \rightarrow \nu_\tau l \nu_l$. However the most important decay channel is the hadron one with a total branching fraction of $\sim 65\%$. Among all the possible hadronic decays as shown on Table 5.2 the ones called "one-prong", where only one charged hadron is produced, are the most frequent.

Decay Mode	Resonance	Mass [MeV]	BF (%)
$\tau^- \rightarrow h^- \nu_\tau$	π	139.6	11.6
$\tau^- \rightarrow h^- \pi^0 \nu_\tau$	ρ	770	26.0
$\tau^- \rightarrow h^- h^+ h^- \nu_\tau$	a_1	1200	9.8
$\tau^- \rightarrow h^- h^+ h^- \pi^0 \nu_\tau$			4.8
other hadronic channels			1.7
total			64.8

Figure 5.2: Hadronic tau decay modes into either one or three charged hadrons h and potential π_0 , and the corresponding branching fractions BF. Also shown are the intermediate resonances and their masses, which are used in some of the tau reconstruction algorithms.

5.3 The Jet reconstruction

6 Search for VBF SUSY in the di- τ_h Like Sign channel

6.1 The Analysis Strategy

The most important aspect of any SUSY analysis is the methodology used to estimate the background contribution in the signal region. The first step consists in the determination of all the irreducible background sources and the definition of an estimation technique for each of the contributions. Four types of background contributions has been considered in this analysis.

The first irreducible background contribution is coming from the Standard Model VBF processes resulting in two τ_h and two jets as shown in Figure 6.1. This background contribution is well modeled being purely electroweak and its cross section is very small. Therefore this background is considered minor and its contribution is directly taken from simulation.

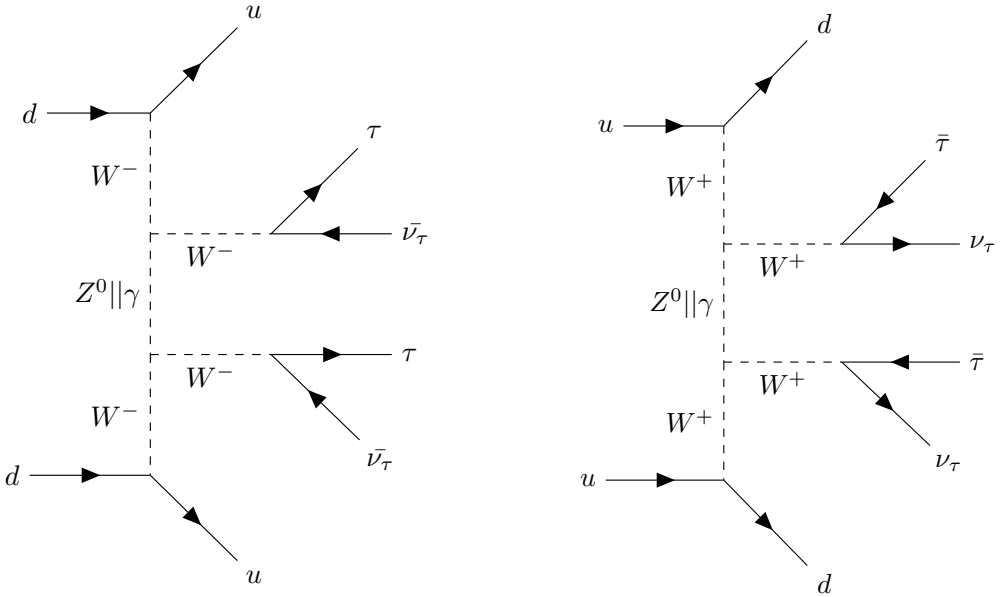


Figure 6.1: Feynman diagrams of irreducible backgrounds of Standard Model Vector Boson Fusion processes with 2 τ_h and 2 jets final state.

Secondly, all the Standard Model VBF processes resulting in three leptons, with one of the leptons, the opposite charged one, failing to pass the tauID, are considered as shown on 6.2.

Those processes are again purely electroweak, therefore their cross section is low and the simulation modeling is expected to be good. Additionally the probability for events coming from this background contribution to pass the event selection is very low. In conclusion,

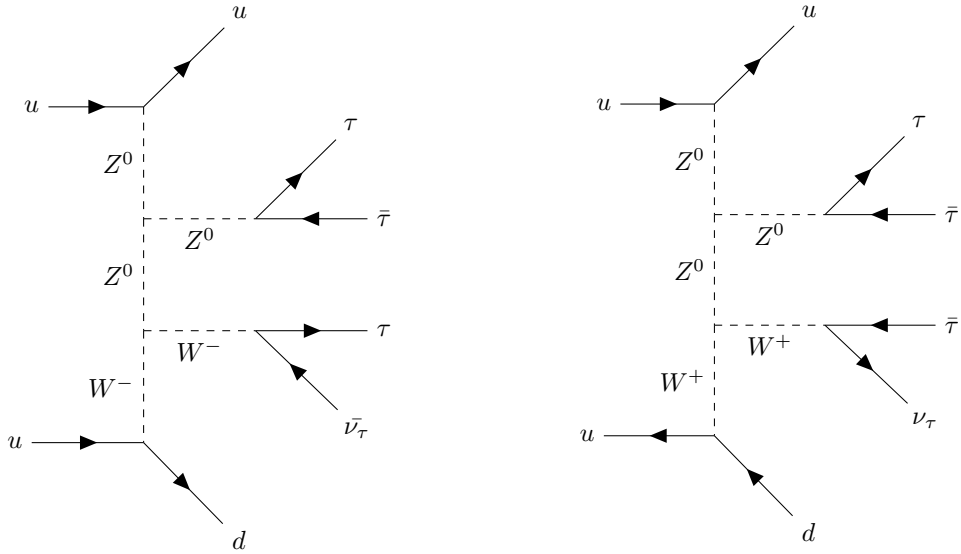


Figure 6.2: Feynman diagrams of irreducible backgrounds of Standard Model Vector Boson processes ending with three τ where the opposite charged one fails to pass the tauID selection criteria.

this topology of events is considered having a minor impact on the total background contribution.

Thirdly, there are the standard model backgrounds where one of the τ_h has a misreconstructed charge as shown in Figures 6.3, 6.4 and 6.5.

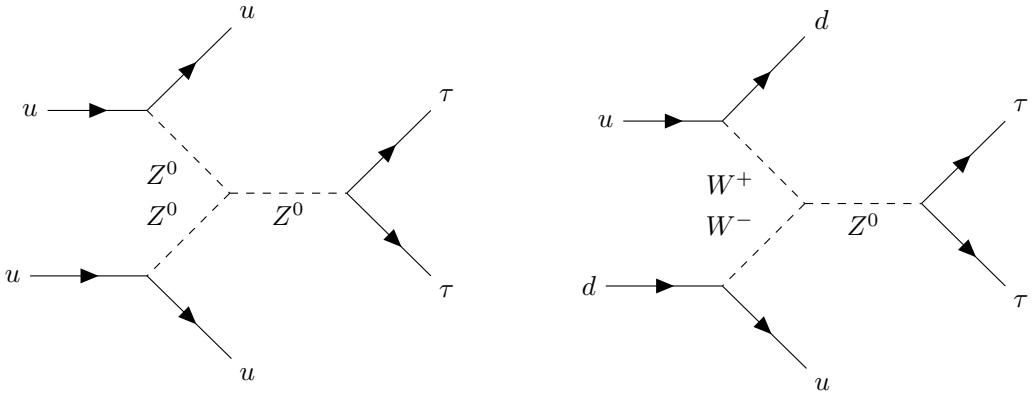


Figure 6.3: Feynman diagrams of irreducible backgrounds of Standard Model Vector Boson Fusion Z^0 production.

All of these processes have a very low cross section compared to the one coming from the main background contribution, therefore those processes are all considered having a minor impact on the background estimation and their event contribution is taken directly

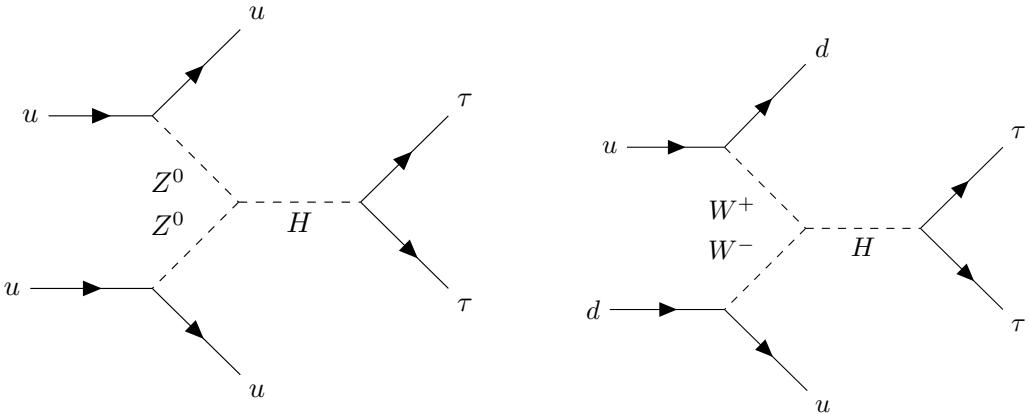


Figure 6.4: Feynman diagrams of irreducible backgrounds of Standard Model Vector Boson Fusion Higgs production.

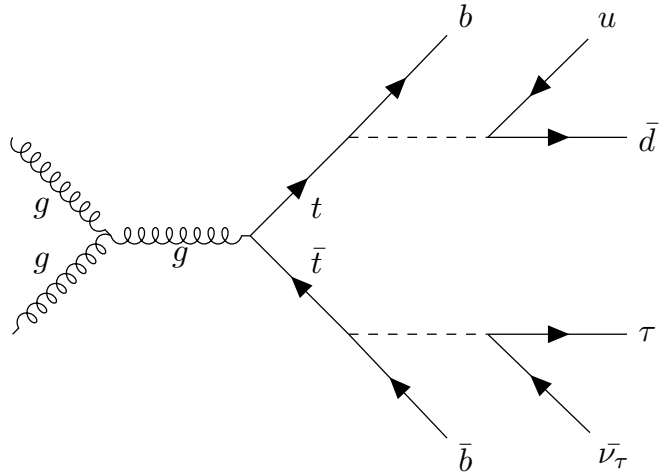


Figure 6.5: Di-leptonic $t\bar{t}$ production where both jets fail the b-tag and one of the τ_h has a mis-reconstructed charge.

from simulation.

The last background contribution comes from all the QCD events resulting in 4 jets with 2 of those jets reconstructed as a fake τ_h . Even though the probability of a jet to fake an τ_h is low the production of QCD events in a hadron collider has huge cross sections. Therefore, even small fake jet- τ_h fake rates from QCD processes, matter. Also, in QCD events, additional jet activity from initial or final jet radiation processes is expected, which gives these type of events a high probability to pass the VBF selection criteria. Those motivations lead to the determination of QCD as main background source for this analysis. Examples of some QCD processes are shown in Figure 6.6 and 6.7.

Similarly to the processes described before there are all QCD processes resulting in 1

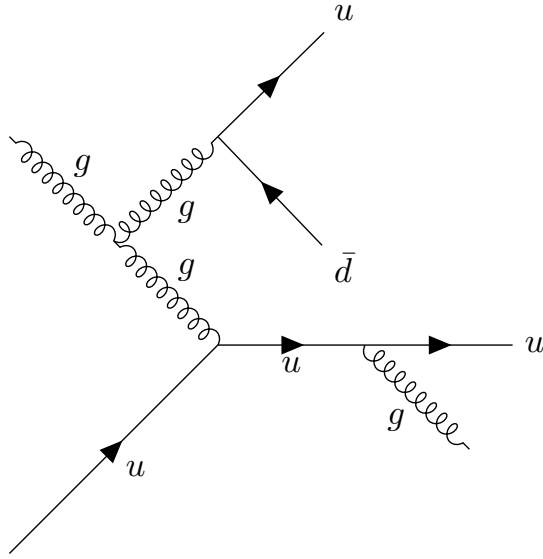


Figure 6.6: Feynman diagrams of a 4 jet QCD production with initial state radiation where 2 jets are misreconstructed as τ_h .

τ_h and 3 jets with one of the jets mis-reconstructed as the second τ_h . Examples of those processes are shown on Figure

The Monte Carlo simulation of QCD events is not reliable due to the complicated modeling of the interactions at the partonic level and the complex fragmentation processes of the resulting jets. Therefore the decision to use a data-driven approach. The number of QCD events in signal region (SR) is estimated directly from data from a defined control region (CR) using the proper correction factor. This correction factor can be properly measured in other exclusive control regions.

The following formula gives a simple description of the whole methodology:

$$N_{SR}^{QCD} = N_{CR}^{DATA} * CF \quad (6.1)$$

where N_{SR}^{QCD} is the number of QCD events predicted in the signal region, N_{CR}^{DATA} is the number of data events in the control region and CF is the correction factor. Further details on the event selection, the data-driven method and the control regions definition is given in the next section.

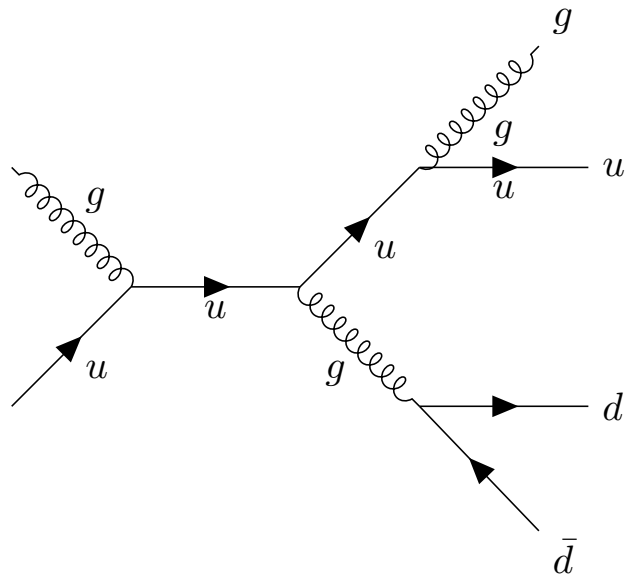


Figure 6.7: Feynman diagrams of a 4 jet QCD production with final state radiation where 2 jets are misreconstructed as τ_h .

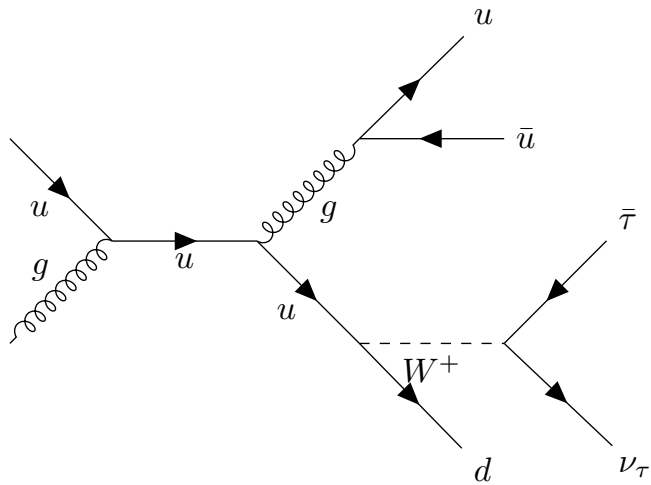


Figure 6.8: Feynman diagrams of W boson plus 3 jets production where 1 jet is misreconstructed as τ_h .

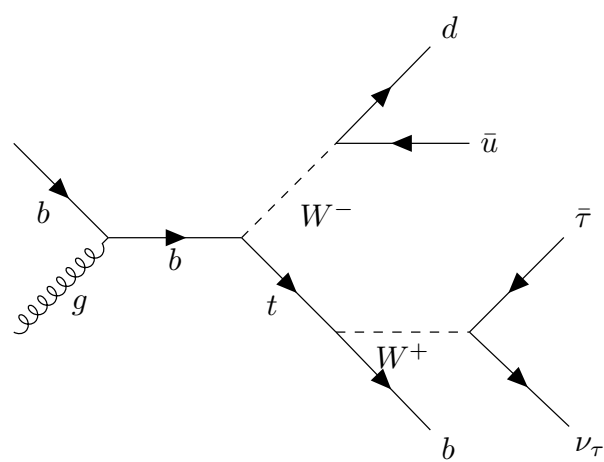


Figure 6.9: Feynman diagrams of single top production where 1 jet is mis-reconstructed as τ_h .

6.1.1 Monte Carlo Samples and Triggers

CMSSW collection label: TriggerResults_HLT
CMSSW type: edm::TriggerResults
<pre>HLT_DoubleMediumIsoPFTau35_Trk5_eta2p1_Prong1_v2 OR HLT_DoubleMediumIsoPFTau35_Trk5_eta2p1_Prong1_v3 OR HLT_DoubleMediumIsoPFTau35_Trk5_eta2p1_Prong1_v4 OR HLT_DoubleMediumIsoPFTau35_Trk5_eta2p1_Prong1_v6 OR HLT_DoubleMediumIsoPFTau35_Trk1_eta2p1_Prong1_v1 OR HLT_DoubleMediumIsoPFTau35_Trk1_eta2p1_Prong1_v3 OR HLT_DoubleMediumIsoPFTau35_Trk1_eta2p1_Prong1_v4</pre>

Table 6.1: List of the required trigger paths.

Process	Official CMS Datasets /DY*/AODSIM
$Z \rightarrow \tau\tau$	ToTauTau_M-20_CT10_TuneZ2star_v2_8TeV-powheg-tauola-pythia6/Summer12_DR53X-PU_S10_START53_V7A-v2
$Z \rightarrow \mu\mu$	ToMuMu_M-20_CT10_TuneZ2star_v2_8TeV-powheg-pythia6/Summer12_DR53X-PU_S10_START53_V7A-v1
$Z \rightarrow ee$	ToEE_M-20_CT10_TuneZ2star_v2_8TeV-powheg-pythia6/Summer12_DR53X-PU_S10_START53_V7A-v1
$Z \rightarrow ll$ ($10 < m_{ll} < 50$)	JetsToLL_M-10To50_TuneZ2Star_8TeV-madgraph/Summer12_DR53X-PU_S10_START53_V7A-v1
$Z \rightarrow ll$ ($m_{ll} > 50$)	JetsToLL_M-50_TuneZ2Star_8TeV-madgraph-tarball/Summer12_DR53X-PU_S10_START53_V7A-v1
$Z \rightarrow ll + 1jet$	1JetsToLL_M-50_TuneZ2Star_8TeV-madgraph/Summer12_DR53X-PU_S10_START53_V7A-v1
$Z \rightarrow ll + 2jets$	2JetsToLL_M-50_TuneZ2Star_8TeV-madgraph/Summer12_DR53X-PU_S10_START53_V7A-v1
$Z \rightarrow ll + 3jets$	3JetsToLL_M-50_TuneZ2Star_8TeV-madgraph/Summer12_DR53X-PU_S10_START53_V7A-v1
$Z \rightarrow ll + 4jets$	4JetsToLL_M-50_TuneZ2Star_8TeV-madgraph/Summer12_DR53X-PU_S10_START53_V7A-v1
$Z \rightarrow ll$ EWK	JJ01JetsToLL_M-50_MJJ-200_TuneZ2Star_8TeV-madgraph_tauola/Summer12_DR53X-PU_S10_START53_V7A-v1

Table 6.2: Drell Yang simulated samples.

Process	Official CMS Datasets /W*/AODSIM
$W + 0$ jets	JetsToLNu_TuneZ2Star_8TeV-madgraph-tarball/Summer12_DR53X-PU_S10_START53_V7A-v2
$W + 1$ jet	1JetsToLNu_TuneZ2Star_8TeV-madgraph/Summer12_DR53X-PU_S10_START53_V7A-v1
$W + 2$ jets	2JetsToLNu_TuneZ2Star_8TeV-madgraph/Summer12_DR53X-PU_S10_START53_V7A-v1
$W + 3$ jets	3JetsToLNu_TuneZ2Star_8TeV-madgraph/Summer12_DR53X-PU_S10_START53_V7A-v1
$W + 4$ jets	4JetsToLNu_TuneZ2Star_8TeV-madgraph/Summer12_DR53X-PU_S10_START53_V7A-v1

Table 6.3: W boson plus additional jets simulated samples.

Process	Official CMS Datasets /TTJets*/AODSIM
tt	MassiveBinDECAY.TuneZ2star.8TeV-madgraph-tauola/Summer12_DR53X-PU_S10_START53_V7C-v1

Table 6.4: Standard model top production simulated sample.

Process	Official CMS Datasets */AODSIM
$WW (\rightarrow 2l2\nu)$	WJetTo2L2Nu_8TeV-powheg-pythia6/Summer12_DR53X-PU_S10_START53_V7C-v1
$W^+ W^+$	/WpWpqq_8TeV-madgraph/Summer12_DR53X-PU_S10_START53_V7A-v1
WW	/WmWmqq_TeV-madgraph/Summer12_DR53X-PU_10.START53_V7A-v1
WW double scattering	/WW_DoubleScattering_8TeV-pythia8/Summer12_DR53X-PU_S10_START53_V7A-v1
WW EWK	/WWjjTo2L2Nu_8TeV_madgraph_qed6_qcd0/Summer12_DR53X-PU_S10_V19-v1
$WZ (\rightarrow 2q2\nu)$	/WZJetsTo2Q2Nu_TuneZ2star_8TeV-madgraph-tauola/Summer12_DR53X-PU_S10_START53_V7A-v1
$WZ (\rightarrow 2l2\nu)$	/WZJetsTo2L2Nu_TuneZ2star_8TeV-madgraph-tauola/_DR53X-PU_S10_START53_V7A-v1
$WZ (\rightarrow 3l)$	/WZJetsTo3L_TuneZ2star_8TeV-madgraph-tauola/Summer12_DR53X-PU_S10_START53_V7A-v1
$ZZ (\rightarrow 2q2\nu)$	/ZZJetsTo2Q2Nu_TuneZ2star_8TeV-madgraph-tauola/Summer12_DR53X-PU_S10_START53_V7A-v1
$ZZ (\rightarrow 2l2\nu)$	/ZZJetsTo2L2Nu_TuneZ2star_8TeV-madgraph-tauola/Summer12_DR53X-PU_S10_START53_V7A-v1
$ZZ (\rightarrow 2l2q)$	/ZZJetsTo2L2Q_TuneZ2star_8TeV-madgraph-tauola/Summer12_DR53X-PU_S10_START53_V7A-v1
$ZZ (\rightarrow 4l)$	/ZZJetsTo4L_TuneZ2star_8TeV-madgraph-tauola/Summer12_DR53X-PU_S10_START53_V7A-v1

Table 6.5: Standard model production of two vector bosons simulated samples.

Process	Official CMS Datasets /VBF */AODSIM
$H \rightarrow WW (\rightarrow 2l)$	HToWWTo2LAndTau2Nu_M-125_8TeV-powheg-pythia6/Summer12_DR53X_S10_START53_V7A-v1
$H \rightarrow ZZ (\rightarrow 2l2\nu)$	HToZZTo2L2Nu_M-120_8TeV-powheg-pythia6/Summer12_DR53X-PU_S10_START53_V7A-v1
$H \rightarrow ZZ (\rightarrow 2l2q)$	HToZZTo2L2Q_M-125_8TeV-powheg-pythia6/Summer12_DR53X-PU_S10_START53_V7A-v1
$H \rightarrow ZZ (4l)$	HToZZTo4L_M-125_8TeV-powheg-pythia6/Summer12_DR53X-PU_S10_START53_V7A-v1
$H \rightarrow ZZ (\rightarrow 4\nu)$	HToZZTo4Nu_M-120_8TeV-pythia6/Summer12_DR53X-PU_S10_START53_V7A-v1
$H \rightarrow \tau\tau$	HToTauTau_M-125_8TeV-powheg-pythia6/Summer12_DR53X-PU_S

Table 6.6: Standard model Higgs production by vector boson fusion simulated samples

Process	Official CMS Datasets /VBF */AODSIM
$bg \rightarrow tW^-$	/T_tW-channel-DR_TuneZ2star_8TeV-powheg-tauola/Summer12_DR53X-PU_S10_START53_V7A-v1
$bg \rightarrow tW^+$	/Tbar_tW-channel-DR_TuneZ2star_8TeV-powheg-tauola/Summer12_DR53X-PU_S10_START53_V7A-v1
$q'b \rightarrow qt$	/T_t-channel_TuneZ2star_8TeV-powheg-tauola/Summer12_DR53X-PU_S10_START53_V7A-v1
$qb \rightarrow qt$	/Tbar_t-channel_TuneZ2star_8TeV-powheg-tauola/Summer12_DR53X-PU_S10_START53_V7A-v1
$qq' \rightarrow tb$	/T_s-channel_TuneZ2star_8TeV-powheg-tauola/Summer12_DR53X-PU_S10_START53_V7A-v1
$qq' \rightarrow tb$	/Tbar_s-channel_TuneZ2star_8TeV-powheg-tauola/Summer12_DR53X-PU_S10_START53_V7A-v1

Table 6.7: Single top simulated samples.

6.1.2 Event Selection

As mentioned in the chapter introduction the di- τ_h channel suffers from huge QCD multijet background, with a rate several orders of magnitude larger than the rate in other channels. Hence this mode, more than any of the others, relies on the efficient background rejection. Fortunately, the VBF and \cancel{E}_T selections provide the required background suppression.

All the collision data events passing the requirements of the triggers shown on Table 6.1 are considered as the interesting events for offline analysis. Similarly to what explained on Section 4.2, the event selection criteria is divided in two distinct parts: the central part, which takes into account the LSP and the decay products of the multiple τ_h , and the VBF part, which cuts over the kinematic properties of the jets coming from a VBF process. The main differences with the other VBF SUSY searches with final states to light leptons, are the substantially tighter τ_h requirements targeting at the suppression of QCD jet background and the looser missing transverse energy (\cancel{E}_T) requirement, to recover some of the signal acceptance lost due to the larger discriminator based on isolation $\tau_h p_T$ thresholds needed to stay efficient with respect to the trigger.

The selected events are required to have at least two Hadron-Plus-Strips (HPS) τ_h with p_T of 45 GeV and a pseudorapidity of $|\eta| \leq 2.1$ in order to ensure that both tracks are reconstructed fully within the acceptance of the tracking system. In addition, a τ_h is required to have exactly one signal charged hadron with $p_T = 5$ GeV. Higher multiplicity τ_h are constrained by the trigger. Each of the τ_h candidates is also required to fulfill the reconstruction and identification criteria described on Table 10.5. Specifically a τ_h candidate is required to pass through a number of discriminators for the proper identification. They are:

- *DecayModeFindingNewDMs*
- *byTightIsolationMVA3newDMwLT*: BDT based tauID discriminator based on isolation, p_T and τ lifetime information, trained on 1-prong, 2-prong and 3-prong τ_h candidates.
- *againstElectronMediumMVA5*: MVA based discriminator to reject electrons faking taus.
- *againstMuonLoose3*: to reject μ faking τ .

The like sign τ_h candidates with the highest p_T and separated from each other by a minimum $\Delta R = 0.3$ are then chosen to form a di- τ_h candidate. Further, to reduce top pair contamination the event is required not to have any jet identified as a b-quark jet by the b-tagging algorithms using the combined secondary vertex loose (CSVL) working point. Only jets with $p_T \geq 30$ GeV and separated from the taus in the $\tau_h\tau_h$ pairs by $\Delta R \geq 0.3$ are searched for b-tags. The higher p_T cut of 30 GeV on b-jets (a looser veto requirement than other analyses with light leptons) allows us to be more efficient with respect to the signal since the higher p_T threshold on taus reduces the contamination of $t\bar{t}$ to a large extent. Further, the event is required to have at least 30 GeV of \cancel{E}_T . All the above described selections is what will be referred as *central* selections.

Subsequently, the following event-wide requirements are imposed. The *VBF selections* are imposed by requiring at least two jets with $p_T = 30$ GeV and absolute pseudorapidity $|\eta| \leq 5.0$. Only jets separated from the leptons in the $\tau_h\tau_h$ pair by $\Delta R \geq 0.3$ are

considered. All jet candidates passing the above requirements and having $|\Delta\eta| \geq 4.2$ and $\eta_1 \cdot \eta_2 < 0$ are combined to form di-jet candidates. The final and the most important of the requirement is an invariant mass of the di-jet candidate, namely m_{jj} , above the threshold of 250 GeV. In order to max the event acceptance the analysis code algorithm takes into account every possible di-jet candidate combination and chooses the one that best passes the VBF requirements and has the highest m_{jj} .

For better visualization and understanding all the selection criteria are summarized the following way:

- **Central selection**

- Trigger: HLT_DoubleMediumIsoPFTau35_Trk*_eta2p1_Prong1_v*
- 2 one-prong hadronically decaying τ with $p_T^\tau \geq 45$ GeV
- $\cancel{E}_T > 30$
- at least 2 jets with $p_T^{jet} \geq 30$ GeV, $|\eta_{jet}| \leq 5$ and loose jetID
- $\Delta R(jet, \tau) \geq 0.3$
- b-tag veto

- **VBF selection**

- $|\Delta\eta(jet, jet)| > 4.2$
- $sign(\eta^{jet1} \cdot \eta^{jet2}) == -1$
- $m_{jj} > 250$ GeV

6.1.3 LS-di-Tau Data-Driven QCD background prediction

The previously introduced estimation method has been developed under the following assumptions:

- 1 all control regions are QCD dominated;
- 2 ϵ_{VBF}^{QCD} is independent from any trigger efficiency concerning τ_h isolation such that each contribution to the numerator and denominator cancels out;
- 3 ϵ_{VBF}^{QCD} is independent from ant MET cut applied in order to reduce QCD background contributions.

Details and results on the validation process done for all the statements is given in Section 6.2.

This method is based on the use of exclusive control regions as shown on Figure 6.11 defined by 2 variables:

1. **Tau Isolation Discriminator:** Each reconstructed τ_h must fulfill the standard object selection criteria as defined on Table 10.5. Additionally, τ' s are separated (classified) using different isolation side bands, namely:
 - a) Tight or T isolated τ_h for `byTightIsolationMVA3newDMwLT`;
 - b) Medium or M isolated τ_h for `byMediumIsolationMVA3newDMwLT` but failed `byTightIsolationMVA3newDMwLT`;
 - c) Loose or L isolated τ_h for `byLooseIsolationMVA3newDMwLT` but failed `byTightIsolationMVA3newDMwLT` and `byMediumIsolationMVA3newDMwLT`.

Each event with a successfully reconstructed LS di- τ pair falls into a exclusive isolation region as shows on Figure 6.10:

- SR or signal region consisting of 2 tight isolated τ_h ;
 - 1T or One Tight isolated τ_h region consisting of one tight isolated τ_h and an additional medium or loose isolated τ_h ;
 - AT or Anti Tight isolation region consisting of at least one medium isolated τ_h and an additional medium or loose isolated τ_h ;
 - AM or Anti Medium isolation region consisting of 2 loose isolated τ_h .
2. **Inversion of the VBF Cuts:** We define a second dimension of exclusivity using VBF cuts described in ???. The regions are defined the following way:
 - a) VBF region: consisting of all the events that passed all VBF cuts previously mentioned;
 - b) VBF inverted region: consisting of all the events that at least fails one of the VBF cuts previously mentioned;

Using these definitions, we define one signal region and 7 control regions, shown in Figure 6.11. In order to keep the QCD background contribution low in signal region and control region 2 an additional cut of MET > 30 GeV is required.

Tight	1T	1T	SR
Medium	AT	AT	
Loose	AM		
τ Isolation	Loose	Medium	Tight
τ Isolation			

SR: Signal region
1T: 1 Tight
AT: Anti Tight
AM: Anti Medium

Figure 6.10: Definitions of the exclusive isolation region depending on the isolation of each of the τ_h where SR is Signal Region consisting of 2 tight isolated τ_h , 1T is One Tight isolated Tau region consisting of one tight isolated τ_h and an additional medium or loose isolated τ_h , AT is Anti Tight isolation region consisting of at least one medium isolated τ_h and an additional medium or loose isolated τ_h , AM is Anti Medium isolation region consisting of 2 loose isolated τ_h

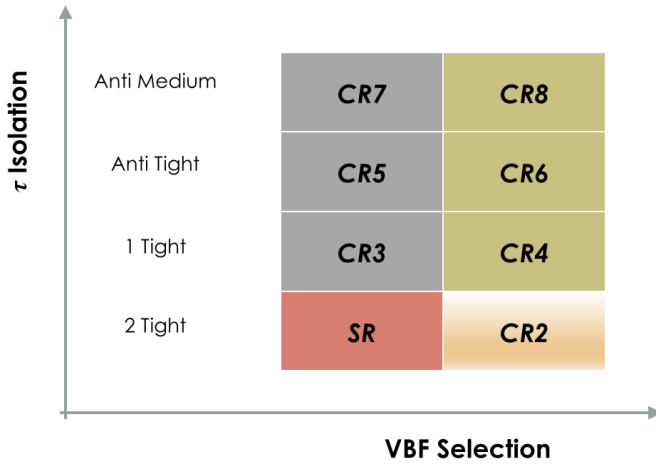


Figure 6.11: Definition of Signal and Control Regions using different τ_h isolation criteria and VBF selection.

The signal and control regions are defined under the assumption of central selection being orthogonal to VBF selection. Figure 6.12 and 6.13 shows the results of the stability study

of M_{jj} shape distribution among different τ isolation sidebands for Data and MC. Further studies are shown in Section ??.

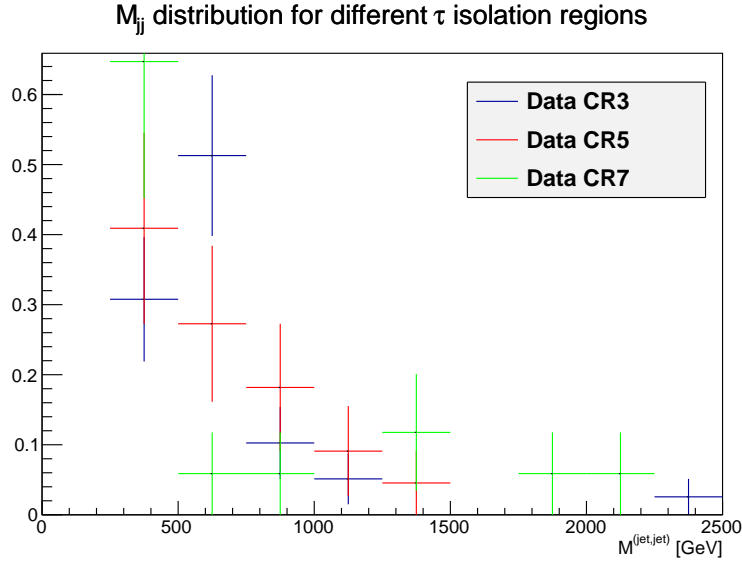


Figure 6.12: M_{jj} shape comparisons among different τ isolation sidebands for Data (CR3, CR5, CR7)

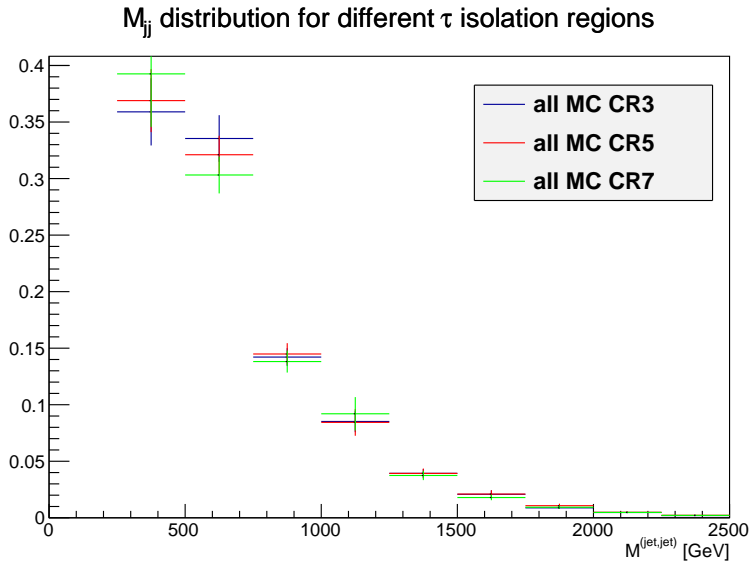


Figure 6.13: M_{jj} shape comparisons among different τ isolation sidebands for all MC contributions (CR3, CR5, CR7)

The estimation of the events in the signal region is done similarly to any other data driven ABCD method by counting the number of events in CR2 (two τ with tight isolation and inverted VBF selection criteria) and multiplying it with a proper conversion factor described in the following equation:

$$N_{SR}^{QCD} = \left(N_{CR2}^{DATA} - N_{CR2}^{\overline{QCD}BG} \right) * \left[\frac{\epsilon_{VBF}^{QCD}}{1 - \epsilon_{VBF}^{QCD}} \right] \quad (6.2)$$

where N_{SR}^{QCD} is the number of QCD events predicted in the signal region, N_{CR2}^{DATA} is the number of data events in control region 2, $N_{CR2}^{\overline{QCD}BG}$ is the number of all non-QCD MC samples events in control region 2 and ϵ_{VBF}^{QCD} is the efficiency of VBF cuts in a given Tau isolation region derived with the following equation.

$$\epsilon_{VBF}^{QCD} = \frac{N_{VBFCR}^{DATA} - N_{VBFCR}^{\overline{QCD}BG}}{\left(N_{VBFCR}^{DATA} - N_{VBFCR}^{\overline{QCD}BG} \right) + \left(N_{\overline{VBFCR}}^{DATA} - N_{\overline{VBFCR}}^{\overline{QCD}BG} \right)} \quad (6.3)$$

where:

- N_{VBFCR}^{DATA} is the number of the events in data for a given τ isolation region and VBF region;
- $N_{VBFCR}^{\overline{QCD}BG}$ is the number of all non-QCD MC events for a given τ isolation region and VBF region;
- $N_{\overline{VBFCR}}^{DATA}$ is the number of events in data in the same isolation Control Region but inverted VBF region;
- $N_{\overline{VBFCR}}^{\overline{QCD}BG}$ is the number of all non-QCD MC events for a given τ isolation region but inverted VBF region.

Three different predictions for the QCD contribution will be given, one for each pair of tau isolation control regions below the two tight isolation. The estimation of the QCD contamination, in the signal region, as shown on Equation 6.2, has two sources of systematics:

- 1 Uncertainty on the generated Monte Carlo samples used in the analysis
- 2 Uncertainty on the stability of the VBF efficiency in regard to a loosening of the tau-identification as previously described in section ??;
- 3 Uncertainty on the stability of the VBF efficiency in regard to a loosening of the \cancel{E}_T cut, since the ϵ_{VBF}^{QCD} is calculated in CRs where no \cancel{E}_T cut is applied.

Systematics for the simulation are estimated by scaling non-QCD contributions by $\pm 50\%$. A systematic error on ϵ_{VBF}^{QCD} is assigned by using the maximal variation among all ϵ_{VBF}^{QCD} measurements in different τ isolation regions with respect to its weighted mean. Similar procedure is done for the assignation of the ϵ_{VBF}^{QCD} coming from \cancel{E}_T cut stability. All the statistical uncertainties are propagated accordingly. Tables 6.8, 6.9 and 6.10 show the event counting for all the control regions previously defined for data and all MC samples. All the numbers except the ones coming from the QCD sample are used as input for the QCD background estimation method. For each of the 3 different τ isolation regions out of the signal region (1T, AT, AM) an independent measurements of ϵ_{VBF}^{QCD} and prediction for N_{SR}^{QCD} is made. Due to low statistics in the τ isolation sidebands the final results will include uncertainties coming from the ϵ_{VBF}^{QCD} stabilities studies on MC shown in section ??.

Sample	Events (SR)	Events (CR2)	Events (CR3)
Data	—	109	39
Drell-Yan	0.037 ± 0.015	1.3 ± 1	0.042 ± 0.0077
VV	0.11 ± 0.065	0.7 ± 0.09	0.035 ± 0.017
W+Jets	0.53 ± 0.04	6.6 ± 0.17	0.83 ± 0.055
Single t	0.036 ± 0.0066	0.25 ± 0.017	0.057 ± 0.008
t <bar>t</bar>	0.11 ± 0.012	1.4 ± 0.051	0.19 ± 0.013
Higgs	$0.0005 \pm 7.2e - 05$	0.012 ± 0.0048	0.0029 ± 0.0023
QCD	8.6 ± 0.61	54 ± 1.2	47 ± 1.9
Total nonQCD MC	0.83 ± 0.079	10 ± 1	1.2 ± 0.06

Table 6.8: Number on events in SR, CR2, CR3 for data and all MC samples used for the estimation of N_{SR}^{QCD}

Sample	Events (CR4)	Events (CR5)	Events (CR6)
Data	737	22	312
Drell-Yan	0.65 ± 0.045	0.002 ± 0.00076	0.029 ± 0.0037
VV	0.6 ± 0.1	0.0031 ± 0.001	0.045 ± 0.015
W+Jets	10 ± 0.2	0.081 ± 0.0096	0.89 ± 0.034
Single t	0.47 ± 0.02	0.011 ± 0.00076	0.1 ± 0.0028
t <bar>t</bar>	2.5 ± 0.059	0.04 ± 0.0024	0.52 ± 0.0095
Higgs	0.012 ± 0.0044	$2.7e - 05 \pm 1.1e - 05$	$0.00018 \pm 2.2e - 05$
QCD	$3.4e + 02 \pm 4$	19 ± 0.68	$1.4e + 02 \pm 1.6$
Total nonQCD MC	15 ± 0.24	0.14 ± 0.01	1.6 ± 0.038

Table 6.9: Number on events in CR4, CR5, CR6 for data and all MC samples used for the estimation of N_{SR}^{QCD}

6.2 Data Driven method validation

Sample	Events (CR7)	Events (CR8)
Data	17	184
Drell-Yan	0.0012 ± 0.00057	0.013 ± 0.0021
VV	0.0011 ± 0.00014	0.033 ± 0.016
W+Jets	0.036 ± 0.0051	0.35 ± 0.015
Single t	0.0061 ± 0.00045	0.058 ± 0.00087
t <bar>t</bar>	0.022 ± 0.00079	0.32 ± 0.0054
Higgs	$4.9e - 06 \pm 2.3e - 06$	$5.7e - 05 \pm 1e - 05$
QCD	15 ± 0.81	$1.1e + 02 \pm 1.7$
Total nonQCD MC	0.067 ± 0.0053	0.77 ± 0.023

Table 6.10: Number on events in CR7 and CR8 for data and all MC samples used for the estimation of N_{SR}^{QCD}

Variable	One Tight region	Anti-Tight region	Anti-Medium
ϵ_{VBF}^{QCD}	0.05 ± 0.008	0.066 ± 0.014	0.085 ± 0.02
N_{SR}^{QCD}	5.2 ± 1	6.9 ± 1.7	9.1 ± 2.5

Table 6.11: Values for ϵ_{VBF}^{QCD} and N_{SR}^{QCD} for different τ isolation regions.

7 Results

7.1 Results

As shown in section 6.1.3 ϵ_{VBF}^{QCD} is calculated for OS and LS. Uncertainties coming from the stability studies on MC shown in section ?? has been taken into account. The weighted average mean coming from the two different measurements gives the following final result:

$$\epsilon_{VBF}^{QCD} = 0.067 \pm 0.0046(stat.)^{-0.00038(MC)+0.0117(\tau iso)+0.0056(MET)}_{+0.00022(MC)-0.0051(\tau iso)+0.0022(MET)} \quad (7.1)$$

Using the following efficiency in Equation 6.2 gives the final QCD background prediction in signal region:

$$N_{SR}^{QCD} = 7.14 \pm 0.92(stat.)^{-0.42(MC)+1.34(\tau iso)+0.64(MET)}_{+0.35(MC)-0.58(\tau iso)+0.25(MET)} \quad (7.2)$$

This final estimate is corrected for the MET bias by taking the central value of the bias as a correction and the uncertainty of the central value as a symmetric uncertainty. The result of this correction is shown in Eq. 7.3

$$N_{SR}^{QCD} = 7.59 \pm 0.92(stat.)^{-0.42(MC)+1.34(\tau iso)+0.20(MET)}_{+0.35(MC)-0.58(\tau iso)-0.20(MET)} \quad (7.3)$$

7.2 Final Yields for LS channel

The LS signal region consist of events satisfying the criteria shown in section ?? with the di- τ charge requirement. As described in section ?? all the backgrounds have been reweighted with τ_h^{fake} reweighting method. Table 7.1 shows the contributions in the signal region from all MC samples and data. QCD is the dominant background and its prediction shown in section 7.1 is compatible with the number in table 7.1. Figure 7.1(a) shows the expected and observed signal rate in bins of E_T . Figure 7.1(b) shows the expected and observed signal rate in bins of M_{jj} . We observe a good agreement in all the distributions range between observed data and the SM prediction. Additional distributions for signal region have been included in the Appendix.

Sample	Events (SR)
Data	9
Drell-Yan	0.037 ± 0.015
VV	0.11 ± 0.065
W+Jets	0.53 ± 0.04
Single t	0.036 ± 0.0066
TTbar	0.11 ± 0.012
Higgs	$0.0005 \pm 7.2e - 05$
QCD Prediction	$7.59 \pm 0.92(stat.)^{+1.38}_{-0.72}(syst.)$
Total nonQCD MC	$0.83 \pm 0.079(stat.) \pm 0.41(syst.)$

Table 7.1: Number on events in SR data and all MC samples. The QCD prediction has been corrected for the unidirectional MET-bias described in section ?? for the combination of the systematic errors.

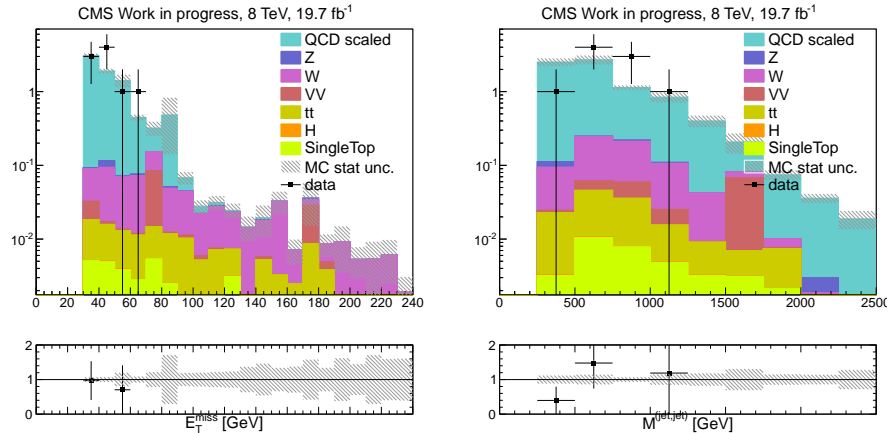


Figure 7.1: (a) E_T and (b) M_{jj} distributions in signal region for Data and all MC samples

7.3 Systematics

The following systematics have been considered:

- **Parton Distribution Functions (PDF):** The systematic effect due to imprecise knowledge of the parton distribution functions is determined by comparing CTEQ6.6L, MSTW2008nnlo, and NNPDF20 PDF with the default PDF and variations within the family of parametrization [?]. The maximal deviation from the central value is used the overall systematic due to PDFs. We obtain a value of 16% on the cross section uncertainty and 23% on the signal acceptance.
- **Initial State Radiation (ISR) and Final State Radiation (FSR):** The systematic effect due to imprecise modeling of initial and final state radiation is determined by re-weighting events to account for effects such as missing a terms in the soft-collinear approach [?] and missing NLO terms in the parton shower approach [?]. We obtain uncertainties of 0.9% and 1.2% for ISR and FSR respectively.
- **Luminosity:** We consider a 2.6% uncertainty on the measured luminosity [?].
- **Trigger, Reconstruction, and Selection:** An overall uncertainty is applied for the trigger uncertainties determined on the correction factors described in AN-12-321 and which are measured using tag-and-probe methods. We consider 6.8% uncertainty per hadronic tau leg [?]. Scale factors for τ_h identification are taken from the tau POG and obtained using a fit of data in a $Z \rightarrow \tau\tau$ enhanced region and fixing the cross section to that measured using ee/ $\mu\mu$. We consider a 100% correlation among the 2 tau legs, therefore we consider 13.6% uncertainty on the signal acceptance.
- **b-Tagging Efficiency:** We consider a 30% uncertainty on the mis-tag rate as measured by the b-tagging POG [?]. For the case of our signal, the systematic uncertainty on the requirement of 0 jets mis-tagged as b-jets is determined by propagating the 30% uncertainty on the mis-tag rate through the following equation (which represents the signal efficiency for requiring 0 jets mis-tagged as b-Jets):

$$\epsilon^{\text{NBtag}<1} = 1 - \sum_{n=1}^N P(n) \cdot \sum_{m=1}^n C(n, m) \cdot f^m \cdot (1-f)^{n-m} \quad (7.4)$$

where $P(n)$ is the probability to obtain n additional jets (non-tau and non-lepton) in the event, $C(n, m)$ the combinatorial of n choose m , and f the mis-tag rate. The probability to obtain at least one additional jet in the event is much less than 1%. Therefore, based on the above equation, the mis-tag rate and uncertainty, and the probability to obtain at least one additional jet we calculate a negligible systematic effect on our signal due to the mis-tag rate.

- **Tau Energy Scale:** We consider the effect of the 3% tau energy scale uncertainty measured by the tau POG on the signal acceptance. The tau 4-momentum is scaled by a factor of $k = 1.03$ ($p_{\text{smeared}} = k \cdot p_{\text{default}}$) and variables are recalculated using p_{smeared} . We find that by using p_{smeared} calculated with a factor of $k = \pm 1.03$, the signal acceptance fluctuates by 4%. Therefore, we assign a 4% systematic on the signal acceptance due to tau energy scale.

- **Jet Energy Scale:** The uncertainty on jet energy correction (JEC) is the result of a factorized approach on $Anti-k_t$ jets with $R = 0.5$ clustered from Particle Flow (PF) candidates. For MC samples JEC is divided in different steps that take into account several levels of correction. The first step consists in a single level of corrections (L1) which estimates the p_t offset in bins of η and N_{PV} for AK5PF jets. The second step, known as MC - Truth Corrections, consists in two levels of corrections (L2 and L3) converging into an η , p_t dependent scaling factor fully derived from MC after applying L1 corrections. The last step takes into account an L5 correction and uncertainties for individual flavors and predefined mixtures inside the reconstructed jets. We assign a 2% systematic on the signal acceptance due to jet energy scale.
- **Jet Energy Resolution:** The measured jet transverse momentum is not necessarily equal to the energy of the original particle due to e.g. a limited detector resolution. This effect is quantified by the jet transverse momentum response R which is defined as $R = p_T/p_T^{particle}$ where p_T denotes the transverse momentum of the jet measured at detector level and $p_T^{particle}$ is the transverse momentum of the original particle-level jet. The average response $\langle R \rangle$ is referred to as jet energy scale and calibrated such that $\langle R \rangle = 1$ for fixed $p_T^{particle}$. The response usually depends on the jet momenta as well as on the pseudorapidity. This is expected since the quality of the jet measurement is directly related to the detector sub-components and the energy of the particles originating e.g. from the track-reconstruction efficiency or the individual amount of detector material. The core of the response is caused by the intrinsic resolution of the various sub-detector components and the precision of the jet clustering algorithms. The response tails are mainly caused by severe jet-mismeasurements. These can be e.g. detector effects like shower leakage or detector noise. Finally, the relative jet transverse momentum resolution is defined as the width of the response distribution corresponding to the gaussian part and hence is a function of p_T and η as well as the total response. One possibility to measure the resolution of the jet transverse momenta in data as well as in simulated events is to utilize the dijet asymmetry A . For events with at least two jets it is defined as:

$$A = \frac{p_{T,1} - p_{T,2}}{p_{T,1} + p_{T,2}} \quad (7.5)$$

For a sufficient number of events the asymmetry is approximately normally distributed and its' standard deviation is σ_A . In an ideal dijet topology the two jets are exactly balanced at particle level which leads to an important relation between the width of the asymmetry σ_A and the jet- p_T resolution $\sigma(p_T)$:

$$\frac{\sigma(p_T)}{\langle p_T \rangle} = \sqrt{2}\sigma_A \quad (7.6)$$

Using the latest JER uncertainty collection from *Summer13_V5_DATA_Uncertainty-Sources_AK5PFchs.txt* assign a 4% systematic on the signal acceptance due to jet energy resolution.

- **MET:** The uncertainty on MET for our signal process is driven by the jet energy scale (non-tau jets) (JES), light lepton energy/momenta scale (LES), and unclus-

tered energy (UCE). The systematic effect from MET due to TES, JES and LES is included in the JES, TES, LES systematic uncertainties described above. We find that a 10% uncertainty on the unclustered energy results in at most a 0.5% fluctuation on the signal acceptance.

Source	Uncertainty	Signal
PDF	—	23%
ISR/FSR	—	1%
Luminosity	2.6%	2.6%
Trigger, ID, Selection	6.8%	16%
Tau Energy Scale	—	4%
b-Jet ID	30%	1%
JES	2% - 10 %	2%
JER	5% - 25 %	4%
MET	10%	0.5%

Table 7.2: Summary of systematic uncertainties

Table 7.2 summarizes all the relevant uncertainties that has been considered.

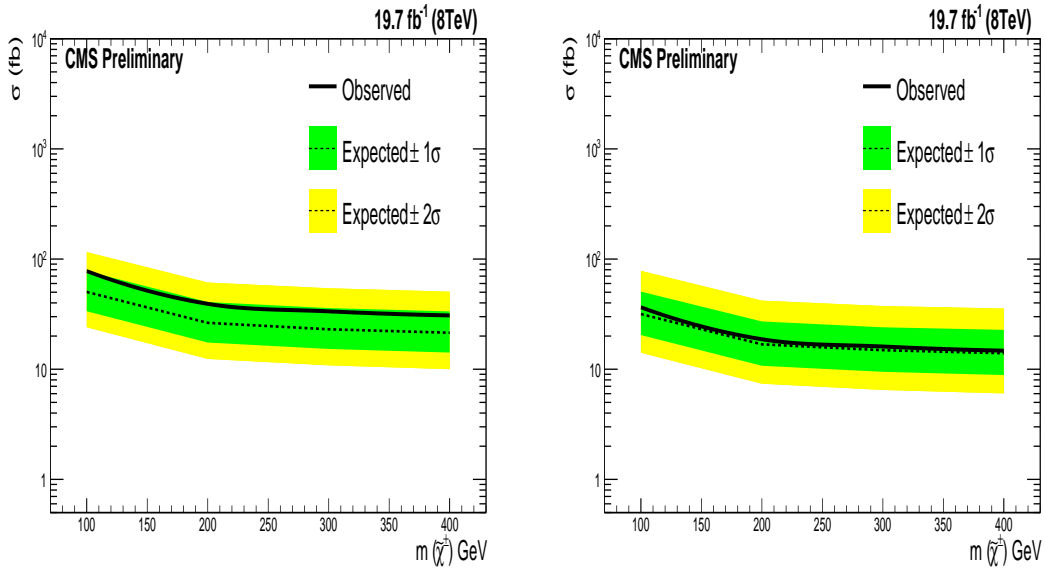


Figure 7.2: Upper limit at the 95% CL on the cross-section as a function of $m_{\tilde{\chi}_2^0} = m_{\tilde{\chi}_1^\pm}$ for the (a) OS $\tau_h \tau_h jj jj$, (b) LS $\tau_h \tau_h jj jj$ final states. The bands represent the one and two standard deviations obtained from the background-only hypothesis.

7.4 Limits

Similarly to what is done in AN-12-321 upper limits at 95% on the cross sections as function of $m_{\tilde{\chi}_2^0} = m_{\tilde{\chi}_1^\pm}$ are set for LS and OS channel. The results are presented using models with a fixed mass for the LSP $m_{\tilde{\chi}_1^0} = 0$ GeV, a $\tilde{\chi}_1^\pm$ mass between $100 \leq m_{\tilde{\chi}_1^\pm} \leq 300$ GeV and a $\tilde{\tau}$ mass of $m_{\tilde{\tau}} = 0.95m_{\tilde{\chi}_1^\pm}$.

Figure 7.2(a) 7.2(b) and shows the upper limit at the 95% CL on the cross-section for OS and LS channel. A combination of the two channels is shown on Figure 7.3. The upper expected limit on $m_{\tilde{\chi}}$ corresponds to the point where the expected limit crosses the theoretical line and is set for $\tilde{\chi}_1^\pm/\tilde{\chi}_2^0$ with masses of 180 GeV. The upper observed limit on $m_{\tilde{\chi}}$ corresponds to the point where the observed limit crosses the theoretical line. We exclude $\tilde{\chi}_1^\pm/\tilde{\chi}_2^0$ with masses below 140 GeV in the models considered. The limit results coming from OS and LS $\tau_h \tau_h jj jj$ final states are combined with other 6 channels documented on AN-12-321 for the final upper limit.

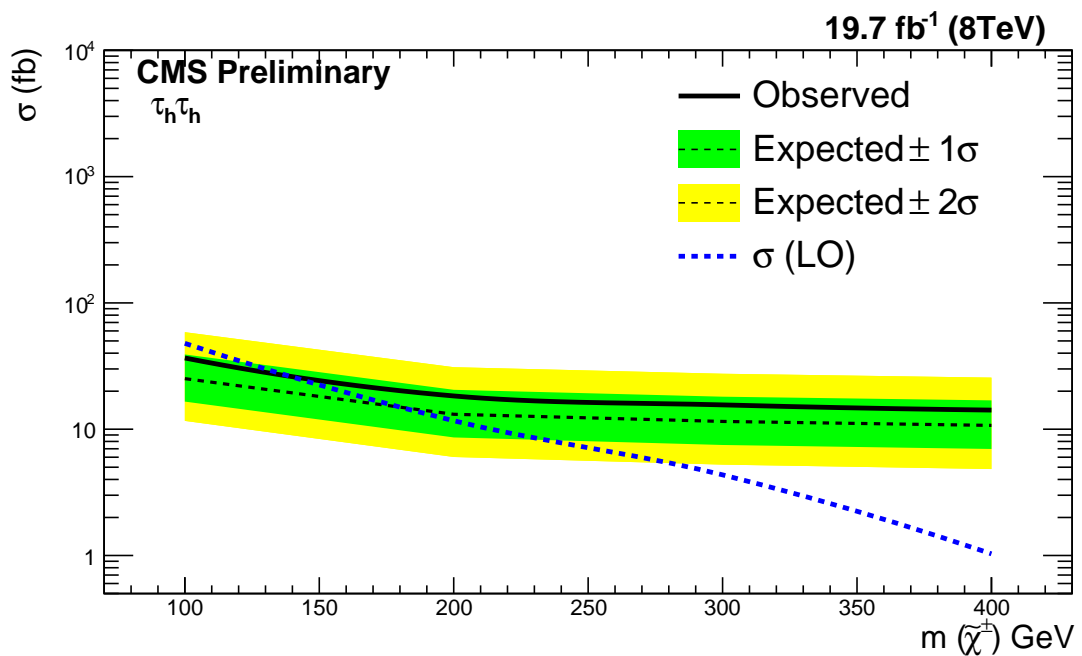


Figure 7.3: Upper limit at the 95% CL on the cross-section as a function of $m_{\tilde{\chi}_2^0} = m_{\tilde{\chi}_1^\pm}$ for the combination of OS and LS $\tau_h \tau_h jj jj$ final states. The bands represent the one and two standard deviations obtained from the background-only hypothesis.

8 SUSY VBF Studies at 13 TeV

9 Conclusion

10 Appendix

10.1 Physic Object Reconstruction

Table 10.1: definition of Vertex.

collection label:	recoVertex
type:	offlinePrimaryVertices
vertex.size()	> 0

10.1.1 Jet Reconstruction

Particle Flow jets (PFJets) are used in this analysis. PFJets use information from all sub-detectors to produce a mutually exclusive collection of particles (namely muons, electrons, photons, charged hadrons and neutral hadrons) that are used as input for the jet clustering algorithms. The anti- k_T clustering algorithm with a reconstruction cone of $R = 0.5$ is used, defined in $\eta - \phi$ ($R = \sqrt{\Delta\eta^2 + \Delta\phi^2}$) [?]. The PFJets used in this analysis are corrected using L1 FastJet, L2 Relative, and L3 Absolute corrections. The L1 FastJet corrections use the event-by-event UE/PU (UE: Underlying Event) densities to remove the additional contributions to the measured jet energies due to underlying event and pile-up particles. The L2 and L3 corrections use jet balancing and $\gamma+$ Jet events to improve and provide a better energy response as a function of p_T and η . This analysis uses the "loose" working point Jet-Id selection criteria. Table 10.3 shows the selection criteria used for the recommended "loose" working point. The efficiency is > 98 for the entire η and p_T range. The "loose" working point has been validated in other studies.

Table 10.2: definition of jets.

collection label:	selectedPatJets
type:	pat::Jet
jet.pt()	$\geq 30.$
fabs(jet.eta())	≤ 5.0
jet.neutralHadronEnergyFraction()	< 0.99
jet.neutralEmEnergyFraction()	< 0.99
jet.numberOfDaughters()	> 1
if(fabs(jet.eta()) < 2.4)	
jet.chargedHadronEnergyFraction()	> 0
jet.chargedEmEnergyFraction()	< 0.99
jet.chargedMultiplicity()	> 0
DeltaR(jet,tau)	≥ 0.3

10.1.1.1 b-Jet Tagging

B-tagged jets are used to reduce $t\bar{t}$ background in the signal region and to obtain $t\bar{t}$ enriched control samples used to estimate the signal rate. This analysis uses the "loose" working point of the combined secondary vertex algorithm. The details of the algorithm can be found in [?]. The EPS13 prescription is used for the b-tagging and mis-tagging scale factors and efficiencies. They are applied using the method called "Event reweighting using scale factors only" https://twiki.cern.ch/twiki/bin/viewauth/CMS/BTagSFMethods#1c_Event_reweighting_using_scale. Table 10.3 shows the selection criteria.

Table 10.3: definition of b -jets.

collection label: selectedPatJets	
type: pat::Jet	
jet.pt()	$\geq 30.$
fabs(jet.eta())	≤ 2.4
DeltaR(jet,tau)	≥ 0.3
jet.bDiscriminator(?)	> 0.244

10.1.2 Tau Reconstruction and Identification

The challenge in identifying hadronically decaying taus is discriminating against generic quark and gluon QCD jets which are produced with a cross-section several orders of magnitude larger. CMS has developed several algorithms to reconstruct and identify hadronically decaying taus based on Particle Flow (PF) objects. For this analysis, the tau POG recommended Hadron Plus Strips algorithm (HPS) is used. HPS makes use of PF jets as inputs to an algorithm that uses strips of clustered electromagnetic particles to reconstruct neutral pions. The electromagnetic strips ("neutral pions") are combined with the charged hadrons within the PFJets to attempt to reconstruct the main tau decay modes outlined in Table 10.4.

Table 10.4: Reconstructed Tau Decay Modes

HPS Tau Decay Modes
Single Hadron + Zero Strip
Single Hadron + One Strip
Single Hadron + Two Strips
Three Hadrons

The single hadron plus zero strips decay mode attempts to reconstruct $\tau \rightarrow \nu\pi^\pm$ decays or $\tau \rightarrow \nu\pi^\pm\pi^0$ decays where the neutral pion has very low energy. The single hadron plus one or two electromagnetic strips attempts to reconstruct tau decays that produce neutral pions where the resulting neutral pion decays produce collinear photons. Similarly, the single hadron plus two strips mode attempts to reconstruct taus that decay via e.g. $\tau \rightarrow \nu\pi^\pm\pi^0$ where the neutral pion decays to well separated photons resulting in two electromagnetic strips. The three hadrons decay mode attempts to reconstruct tau decays that occur via $\rho(770)$ resonance. In all cases, electromagnetic strips are required

to have $E_T > 1 \text{ GeV}/c$. Additionally, the particle flow charged hadrons are required to be compatible with a common vertex and have a net charge of $|q| = 1$.

In order to enforce the isolation requirement on the reconstructed tau, a region of size $R = 0.5$ around the tau decay mode direction is defined. Any PF candidates not used for the reconstruction of electromagnetic strips and charged hadrons not involved in the reconstruction of the tau decay modes are used to calculate isolation. The "Tight" mva isolation (with lifetime) working points are used to define the signal regions.

In order to discriminate against muons, HPS taus are required to pass the lepton rejection discriminator which requires the lead track of the tau not be associated with a global muon signature. In order to discriminate against electrons, HPS taus are required to pass a MVA discriminator which uses the amount of HCAL energy associated to the tau with respect to the measured momentum of the track (H/p). Additionally, the MVA discriminator considers the amount of electromagnetic energy in a narrow strip around the leading track with respect to the total electromagnetic energy of the tau. Finally, HPS taus must not reside in the ECAL cracks. In all channels, the identification and isolation used follows the Tau POG recommended criteria. The exact discriminator names and working points for each channel are listed and described in their respective sections. Table 10.3 shows the selection criteria for τ leptons.

Table 10.5: definition of τ leptons.

collection label: patTaus	
type: pat::Tau	
fabs(tau.eta())	<= 2.1
tau.pt()	>= 45.0
tau.leadPFChargedHadrCand()->pt()	>= 5.0
tau.tauID(''byTightIsolationMVA3newDMwLT'')	> 0.5
tau.tauID(''byMediumIsolationMVA3newDMwLT'')	> 0.5
tau.tauID(''byLooseIsolationMVA3newDMwLT'')	> 0.5
(decayModeFindingNewDMs	> 0.5 &&
signalPFChargedHadrCands().size()	== 1)
tau.tauID(''againstElectronMediumMVA5'')	> 0.5
tau.tauID(''againstMuonLoose3'')	> 0.5

Table 10.6: definition of \cancel{E}_T

collection label: patMET
type: patPfMetT0pcT1Txy

10.2 Physic Object Reconstruction at 13 TeV